Experimental characterization, parameter identification and numerical sensitivity analysis of a novel hybrid sensible/latent thermal energy storage prototype for industrial retrofit applications

Lukas Kasper [a],*, Dominik Pernsteiner [b], Alexander Schirrer [b], Stefan Jakubek [b], René Hofmann [a]

[a] *TU Wien, Institute of Energy Systems and Thermodynamics, Getreidemarkt 9/BA, 1060 Vienna, Austria*
[b] *TU Wien, Institute of Mechanics and Mechatronics, Getreidemarkt 9/BA, 1060 Vienna, Austria*

GRAPHICAL ABSTRACT

First-of-a-kind industrial steam storage retrofit with phase change material

First prototype of a novel hybrid thermal energy storage concept
- Combination of Ruths steam storage (RSS) and latent heat thermal energy storage (LHTES)
- Easy, reversible retrofit procedure to meet industrial requirements
- Economic option for increasing storage
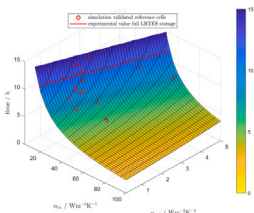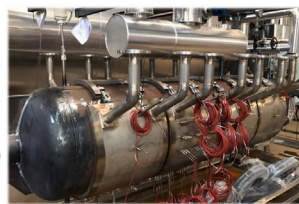- Could leverage the advantages of both storage types
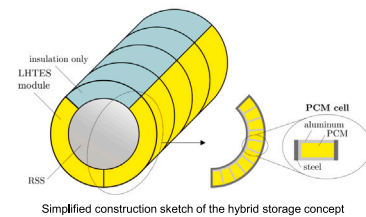
Experimental investigation of operational behaviour
- Real measurement results during operation in an industrial steel plant
- Storage operation between 150°C and 220°C
- Storage capacity increase by 30%
- Charging/discharging times of 10.4/8.6 h

Numerical modelling and detailed sensitivity analysis
- Heat transfer between RSS and LHTES is critical to performance
- Potential to reduce charging/discharging times 10-fold
- Flexible LHTES modules are proposed for future improvement of hybrid storage

Simplified construction sketch of the hybrid storage concept

Storage prototype before insulation installment

Charging duration sensitivity in dependence of outer heat transfer values of LHTES modules

ARTICLE INFO

ABSTRACT

Hybrid design combinations of sensible and latent heat thermal energy storage (TES) leverage the advantages and reduce the disadvantages of both types. Thus, the range of application of said individual storage types is extended and crucial retrofit opportunities are enabled. Such hybrid TES concept consisting of a Ruths steam storage (RSS) and a surrounding layer of storage containers filled with an eutectic mixture of sodium nitrate ($NaNO_3$) and lithium nitrate ($LiNO_3$) as phase change material (PCM) was for the first time realized and investigated during operation in a steel production plant.

In this work, the hybrid TES prototype is characterized with the help of detailed modelling and real measurement results. Uncertain model parameters are identified via parameter optimization and the numerical models show satisfactory validation results. Additional 30% of thermal energy could be stored in the PCM containers retrofitted to the lab-scale RSS. Charging/discharging times and specific thermal power of the PCM containers were roughly measured as 8 h and 12 h and $560\,kWm^{-3}/-802\,kWm^{-3}$, respectively, in the typical operation region. A sensitivity analysis of the performance indicators reveals potential but also engineering challenges for following generations of the hybrid TES concept. Compared to the achieved experimental results, charging/discharging power could be increased by up to 10 and 5 times, respectively, in the future by adequate measures to increase heat transfer between both storage types.

Nomenclature

Acronyms

LHTES	Latent Heat Thermal Energy Storage
PCCs	Phase Change Composites
PCM	Phase Change Material
RMSE	Root Mean Square Error
RSS	Ruths Steam Storage

Indices

alu	aluminium
i	index in sum
L	liquid
n	number of simulation/ measurement values
S	solid
stl	steel
in	inner value
lower	lower sensor positions of Type A instrumentation
out	outer value
ref	reference
upper	upper sensor positions of Type A instrumentation

Parameters and Variables

α	heat transfer coefficient $\left(\mathrm{W\,m^{-2}\,K^{-1}}\right)$
β	volumetric thermal expansion coefficient $\left(\mathrm{K^{-1}}\right)$
ΔH	enthalpy difference (J)
Δl_m	specific latent heat $\left(\mathrm{kJ\,kg^{-1}}\right)$
Δt	time step (s)
Δx_{PCM}	cavity PCM dimension in x direction (m)
Δy_{PCM}	cavity PCM dimension in y direction (m)
Δmass	mass difference (kg)
$\dot{m}$	mass flow (kg/s)
$\dot{Q}$	heat flux (W)
ϵ	mushy region temperature range (K)
$\hat{T}$	simulated temperature
$\mathbf{f}$	force density $\left(\mathrm{kg\,m^{-2}\,s^{-2}}\right)$
$\mathbf{g}$	gravitational acceleration vector $\left(\mathrm{m\,s^{-2}}\right)$
$\mathbf{q}$	specific heat flux $\left(\mathrm{W\,m^{-2}}\right)$
$\mathbf{u}$	velocity vector $\left(\mathrm{m\,s^{-1}}\right)$
μ	dynamic viscosity $\left(\mathrm{N\,s\,m^{-2}}\right)$
ϕ	inclination angle
ρ	density $\left(\mathrm{kg\,m^{-3}}\right)$
ρ_0	constant density of PCM $\left(\mathrm{kg\,m^{-3}}\right)$
$\sigma()$	error band (standard deviation)
θ	uncertain parameters (optimization variable)
$\bar{\theta}$	solution of optimization problem
c	specific heat capacity $\left(\mathrm{J\,kg^{-1}\,K^{-1}}\right)$
H	enthalpy (J)
h	specific enthalpy $\left(\mathrm{J\,kg^{-1}}\right)$
$J(\theta)$	objective function

k	thermal conductivity $\left(\mathrm{W\,m^{-1}\,K^{-1}}\right)$
L_x, L_y	length of PCM segment in x,y direction (m)
p	absolute pressure $\left(\mathrm{N\,m^{-2}}\right)$
T	temperature (°C)
t	time (s)
T_m	melting temperature (°C)
u, v	velocity components in x, y direction $\left(\mathrm{m\,s^{-1}}\right)$
V	volume of RSS $\left(\mathrm{m^3}\right)$
x, y	space coordinates (m)

Symbols

$D, \partial D$	spatial domain, boundary of spatial domain
∇	Nabla operator: $\nabla = (\partial/\partial x, \partial/\partial y)$

1. Introduction

1.1. Motivation

Due to the substitution of fossil fuels with intermittent renewable energy sources, a substantial increase in energy storage capacity is needed worldwide over the next years [1]. In this context, thermal energy storage (TES) is in focus due to its ability to balance thermal energy supply with consumption, allowing to overcome the problem related to the intermittency of renewables, and increasing the efficiency and the flexibility of energy systems [2–4]. Hence, research on TES has experienced a rapid increase in terms of numbers of publications [5].

Despite considerable research effort in this field, integration of TES technology in industry is not straightforward, since short payback time and profitability are key criteria for investment decisions [6] and high initial capital cost is a major impediment [7–9]. Furthermore, due to their individual advantages and disadvantages, the applicability of storage technologies strongly depends on the process requirements and technical restrictions such as available conversion technologies and thermodynamic constraints [6]. Typically, process technologies and energy supply systems have long lifetimes of several years to decades [10]. However, process requirements change more frequently. Thus, retrofit approaches which feature small changes in the infrastructure of the energy system have special relevance for the current transition phase [11].

1.2. Background

Steam systems are a part of almost every major industrial process today [12]. Worldwide, steam systems account for approximately 30 % of the energy used in manufacturing facilities [13], which in turn are accountable for nearly a third of the world's energy consumption [14]. Even small increases in efficiency of steam systems can thus account for considerable energy savings on a global scale. Here, TES integration and expansion is a viable solution to increase flexibility and efficiency of industrial plants [3,4,7,15] and is available for various temperature and pressure ranges.

* Corresponding author.
  E-mail address: lukas.kasper@tuwien.ac.at (L. Kasper).

1.2.1. Ruths steam storage

The Ruths steam storage (RSS) is a well-known and widely applied sensible TES type in industrial steam systems [16–19]. The RSS is a pressure vessel containing a two-phase mixture of liquid water and steam, which is directly charged and discharged with steam [20]. Thus, the storage medium is equal to the heat transfer medium and no heat exchangers are required. During charging of the storage tank, the incoming steam partly condenses, which leads to an increase in the liquid filling level, pressure and temperature. During discharging, the saturated steam contained in the storage tank is extracted, causing a decrease of pressure, temperature and liquid filling level to maintain a thermodynamic equilibrium in the vessel [21,22].

The fast reaction time and high charging and discharging rates are considered as main advantages of the RSS [16,17]. However, steam pressure in an RSS drops during discharging. Options to avoid such pressure drop, which is disadvantageous for some applications, include the integration of an external flash evaporator and integration of phase change material (PCM) inside the storage vessel [16]. A further disadvantage of RSS is that its storage capacity is always determined by vessel volume and the allowed system pressure operation range. Thus, no capacity expansion is possible in the case of increased requirements during the storage life time. Furthermore, acquiring additional RSS units is rather expensive with the price being mainly driven by the pressure vessel costs at high temperatures [6]. This highlights the necessity for cost-efficient alternatives.

1.2.2. Latent heat thermal energy storage

Amongst all TES technologies, latent heat thermal energy storage (LHTES) are currently the most studied category in the literature [5]. LHTES primarily consist of a heat exchanger, which transfers energy between a heat transfer fluid and phase change material (PCM). PCM can store a large amount of energy during, typically liquid–solid, phase change within a small temperature range. This nearly isothermal charging/discharging process together with its high energy density compared to sensible TES is often considered as major advantage of LHTES over the latter [23]. However, while many materials have been considered and studied for use in LHTES, only few of them reached the stage of commercial application [24–28]. Underlying problems, which have not yet been fully overcome, include phase separation, subcooling, corrosion, long-term stability, and low heat conductivity [29]. The most critical disadvantage with regards to TES performance is the low thermal conductivity of most PCM [23]. In the scientific literature, various methods have been presented for increasing the heat transfer between the heat transfer medium and PCM [30]. Prominent strategies include adding fins or other extended surfaces [31–34], heat pipes [35], porous media [36], or nanoparticles [37,38] into PCM. Among various high-conductivity fillers, carbon-based porous materials, such as carbon/graphene based foam [39] and aerogel [40,41] carbon nanotube sponge [42] and expanded graphite [43] are frequently adopted to improve the thermal conductivity of PCMs by fabricating phase change composites (PCCs) [44]. For recent review articles on the topic of heat transfer enhancement for PCM containers, see, for example [45]. Furthermore, we refer to a comprehensive recent review on metal-, carbon-, and ceramic-based PCCs by Wu et al. [46]

1.2.3. Hybrid storage approaches

As mentioned above, each TES type exhibits advantages and disadvantages depending on the specific application [11]. This fact motivates the basic idea to combine both sensible and latent heat TES to leverage the advantages and reduce the disadvantages of both types.

Some combinations of sensible water storage with PCM have been proposed in literature. E.g., Abdelsalam et al. [47] and Zhao et al. [48] numerically investigated the integration of PCM modules inside a liquid water storage, showing promising increase in energy storage capacity and charging rates. Frazzica et al. [49] pursued a similar approach by testing macro-encapsulated PCMs added to water storage. Underwood

et al. [50] evaluated a hot water storage tank enhanced by PCM encapsulated in pipe coils and Cabeza et al. [51] experimentally tested the addition of PCM at the top of a stratified hot water storage. Zauner et al. [52] presented a hybrid sensible/latent heat storage system in the form of an inverted shell-and-tube configuration, where PCM was arranged in tubes, and thermal oil was used as sensible storage and as heat transfer medium.

Besides sensible water storage, often found in the building sector [49,53], also examples of hybrid steam/PCM storage, more relevant for industrial application, can be found in literature. The arrangement of pressure-resistant PCM capsules inside the RSS pressure vessel was mentioned by Steinmann & Eck [16], Buschle et al. [54] and Tamme et al. [55]. Another proposed option is to use a tube register surrounded by PCM to extend the RSS [54,55]. Buschle et al. [54] found that the tube register arranged outside the pressure vessel provides better results in terms of solidification time than the arrangement at the internal side of the pressure vessel.

A novel hybrid storage concept was proposed by Dusek & Hofmann [56,57] in 2018. Therein, PCM filled containers are placed at the shell surface of the RSS. The authors state that this configuration combines the high charging and discharging rates of the RSS and the high energy density of PCM. It is also possible to divide the outer PCM containers into several chambers, enabling the arrangement of PCM with different material properties [58]. Such mixture can lead to increased charging rate [59,60] in LHTES. Furthermore, the concept of Dusek & Hofmann [58] considers the integration of electrical heating elements or heat exchangers inside the PCM containers. The authors state that placing these inside the PCM instead of the RSS is advantageous, since pressure increase in the RSS is reduced and delayed. Such power-to-heat options are expected to become an increasingly relevant and cost-effective technology, especially at high temperature levels [61].

Niknam & Sciacovelli [62] presented the first holistic techno-economic investigation of the hybrid storage concept proposed by Dusek & Hofmann [56,57]. They provided calculation and comparison of total costs by including capital expenditures (CAPEX), annual fuel and non-fuel related operating costs and also taking technology lifetime into account. This investigation resulted in CAPEX of the hybrid storage system that are 5 % less than the case with a conventional RSS and additional relative operational savings of about 5.5 %, thus confirming the results of Hofmann et al. [63] that such hybrid storage can be advantageous and cost-effective. However, while their analysis is based on a dynamically modelled RSS/LHTES system, the modelling approach includes several simplifications. For example, the LHTES part is only modelled in one dimension, and, more critically, perfect heat transfer between both storage types is assumed.

1.3. Scope of this investigation

In this work, the novel hybrid sensible/latent TES prototype first proposed by Dusek and Hofmann [56,57] is experimentally investigated. In our previous work, a model of the hybrid storage was established and the RSS model was validated with data from an industrial plant [58]. Furthermore, a non-linear design optimization tool for such hybrid storage system was developed by Hofmann et al. [63] to enable cost-effective retrofitting of conventional RSS. A detailed simulation study of different hybrid storage PCM arrangements were compared and presented in Dusek et al. [64]. A detailed numerical simulation model of the PCM containers was established [65] and in-depth parameter studies on the influence of natural convection under inclination on optimal aluminium proportions and fin spacings were carried out [66]. In addition, we established a co-simulation methodology for the hybrid storage prototype [67], followed by work on data-based model reduction [68] and state estimation of nonlinear LHTES problems [69] to allow for optimal operational control of LHTES and hybrid sensible/latent TES storage.

To further assess this hybrid RSS/LHTES retrofit concept, the first-of-a-kind prototype was constructed and investigated during operation in a steel plant. In this work, the hybrid TES prototype is characterized with the help of real measurement results and detailed numerical simulations.

Based on the state of the art outlined above, the main contributions of this article are as follows:

- We conducted the first experimental characterization of a novel hybrid sensible/latent thermal energy storage prototype for industrial retrofit applications.
- We successfully validate developed numerical models of the hybrid storage and identify uncertain numerical model parameters via experimental data.
- We characterized key performance values of the novel hybrid storage such as retrofitted storage capacity, charging/discharging duration and power.
- We performed a sensitivity analysis of parameters critical to the hybrid storage performance, and reveal potential for future improvement.
- Our analysis presents essential guidelines for future development of hybrid storage applications.

1.4. Paper structure

After this introduction, this paper is organized as follows: Section 2 presents the experimental setup, numerical modelling and analysis methods used in this study. The results of experimental and numerical investigations are given in Section 3. In Section 4, the main findings are highlighted and critically assessed. Furthermore, specific suggestions for further research are emphasized.

2. Methods

In this chapter, the experimental setup, numerical modelling and analysis methods used in this study are presented.

2.1. Problem statement

In the proposed hybrid storage concept by Dusek & Hofmann [56, 57], introduced in Section 1.3, PCM filled containers are placed at the shell surface of an RSS. Fig. 1 illustrates a simplified construction sketch of a possible realization. However, to enable industrial exploitation, the actual design is bound to a number of thermodynamic, economic and safety requirements. In a recent review, Gasia et al. [70] established more than 25 requirements for both sensible and latent heat TES to handle in order to ensure optimal performance and further achieve widespread deployment. These can be grouped into chemical, kinetic, physical and thermal (from a material point of view) and environmental, economic and technological (from both material and system points of view) [70]. Naturally, optimization of all of these, partly opposing, aspects is impossible and trade-offs have to be tolerated. Our most important considerations are given in the following list.

- The LHTES retrofit should increase the effective thermal energy storage capacity while reducing investment costs compared to equivalent additional RSS capacity. This is only possible without interfering with existing steam infrastructure.
- Thermal heat transfer between RSS and LHTES should be optimized to maximize charging/discharging power and efficiency.
- Both material configuration and mechatronic setup should allow adequate control over the TES, to optimize its operation within the operating conditions.
- The retrofit construction must not permanently modify the RSS and must allow access to the pressure vessel's internal and external surface area under reasonable effort. This is necessary to allow for mandatory recurrent inspection at an interval of five to ten years.

- Material choice and construction design should ensure durability (i.e. no corrosion or deformation) and workplace safety (i.e. no toxicity, fire and explosion hazard).

When it came to the last item in the above list, i.e. ensuring durability and safety of the construction design, there were two main issues:

- Corrosion effects: It was found that corrosion occurs especially when in contact with water, e.g., humid air. Therefore, also the purity of the used PCM is of importance and direct contact of the PCM and the RSS pressure vessel was disregarded because of safety concerns.
- Thermal expansion: the thermal expansion of $NaNO_3$-$LiNO_3$ was determined in small-scale experiments and resulted in 14 to 17% between 25 and 220 °C, which would result in high stresses in a closed-container design.

While carefully assessing all technical decision criteria and also budgetary restrictions, we arrived at a first prototype design as described in Section 2.2.1. Detailed reasoning on the design choices for the here investigated prototype exceed the scope of this contribution and we refer to the project's public report for further information [71].

2.2. Experimental design and setup

Experimental investigations of the dynamic behaviour of the hybrid storage device were conducted at the steel production facility of voestalpine Stahl Donawitz GmbH, located in Leoben, Austria. The lab-scale storage tank, described in detail in Section 2.2.1, is charged with steam via the discharge pipe of one of the 80 m^3 industrial size RSS vessels operated on site. Discharging takes place against ambient pressure.

2.2.1. The hybrid storage prototype

A fully functional lab-scale RSS was constructed to replicate the behaviour of a typical industrial-size RSS while reducing prototype cost to a minimum. It consists of a cylindrical pressure vessel with hemispherical sides. A steam lance with a series of injecting nozzles is located inside the base vessel body for charging. A typical steam collector is located on top of the base body for discharging. All relevant geometry parameters are given in Table 1.

Eight LHTES container modules, four on each side of the vessel, were constructed to mount onto the RSS. Fig. 1 shows a concept sketch of their positioning. During discharging, the top part of a horizontal steam storage vessel contains dry steam, which has a very poor heat transfer coefficient of $10 \, W \, m^{-2} \, K^{-1}$, which is 70 times smaller than that of liquid water . Hence no reasonable heat transfer rates between RSS and LHTES can be achieved [67]. Therefore, the modules of the hybrid storage are not forming a full half-circle (corresponding to maximum storage capacity), but instead only surround the vessel to an angle of 133.5° from the bottom, leaving the rest to be insulated. To find the most economically efficient share of LHTES module coverage, the combined behaviour of the hybrid system must be studied under operating conditions. For this purpose, we provided a co-simulation methodology in our previous work, see Pernsteiner et al. [67].

LHTES modules are made from stainless steel (1.4571) with a wall thickness of 3 mm. Inside, an aluminium fin structure is installed, orientated in the radial-axial plane of the RSS. The relevant geometry parameters are also given in Table 1. A concept was developed to exhaust any gases, that may escape the liquefied PCM, from the installation hall. It consists of a 32 mm reinforced polyurethane hose which connects two DN50 flanges from each of the 8 modules. The PCM modules were tightened to the RSS with metallic springs up to a pre-calculated permissible force. This should ensure direct contact between the RSS surface and the PCM modules and reduce separation occurring due to dissimilarity of the steels and construction imprecisions. Major
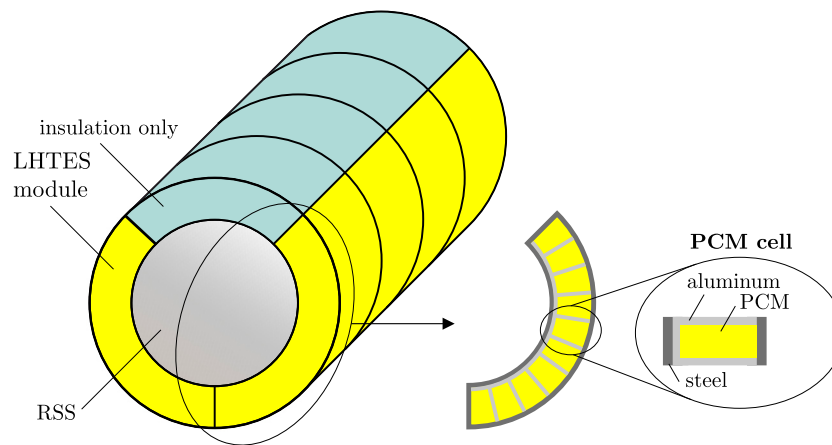
Fig. 1. Simplified construction sketch of the hybrid storage. PCM modules are attached to the cylindrical steam storage up to an angle of 133.5° from the bottom. The modules consist of a stainless steel shell and an aluminium fin structure in the radial-axial plane, thus forming multiple separated PCM cells. Note: sketch is not true to scale.

Table 1
Relevant geometry parameters of the hybrid storage prototype.

RSS pressure vessel	
Material	Steel (P235GH)
Outer diameter	711 mm
Wall thickness	12.5 mm
Cylindrical length	2319 mm
Dished ends wall thickness	15 mm
Dished ends height	186 mm
LHTES container modules	
Wall material	Stainless steel (1.4571)
PCM	LiNO$_3$-NaNO$_3$
Width (outer dimension)	545 mm
Inner radius	355.5 mm
Height of PCM layer (radial to RSS)	30 mm
Wall thickness (lateral)	5 mm
Wall thickness (inner, outer, top, bottom)	3 mm
RSS angle covered	133.5°
Number of modules	8
PCM mass per module	19.52, 19.58, 19.83, 19.03, 19.00, 19.61, 19.74, 19.83 kg
Aluminium fins	
Fin material	Aluminium (AW-6060T66)
Fin number per module	85
Fin thickness	2 mm
Fin height	29.5 mm
Fin spacing	10 mm
Insulation	
Insulation material	Mineral wool
Thickness	100 mm

Table 2
Relevant material properties of LHTES prototype.

Property		PCM (LiNO$_3$-NaNO$_3$)	Aluminium (AW-6060T66)	Steel (Stainless 1.4571)
density	$\dfrac{\rho}{\mathrm{kg\,m^{-3}}}$	2317 [72]	2700 [73]	8000 [74]
spec. heat capacity	$\dfrac{c}{\mathrm{J(kg\,K)^{-1}}}$	1350 (S) [72] 1720 (L) [72]	910 [73]	500 [74]
heat conductivity	$\dfrac{k}{\mathrm{W(m\,K)^{-1}}}$	0.87 (S) [72] 0.575 (L)[a]	237 [73]	15 [74]
melting temperature	$\dfrac{T_m}{{}^\circ\mathrm{C}}$	192[b]	–	–
mushy region temperature range	$\dfrac{\epsilon}{{}^\circ\mathrm{C}}$	0.4[b]	–	–
spec. latent heat	$\dfrac{\Delta l_m}{\mathrm{kJ\,kg^{-1}}}$	309.1[b]	–	–
thermal expansion coefficient	$\dfrac{\beta}{\mathrm{K^{-1}}}$	$3.5 \cdot 10^{-4}$[c]	–	–
dynamic viscosity	$\dfrac{\mu}{\mathrm{N\,s\,m^{-2}}}$	$5.8 \cdot 10^{-4}$[c]	–	–

[a] Average value from literature [72] and [55].
[b] Value from measurement at AIT Austrian Institute of Technology GmbH (accredited laboratory - EN ISO/IEC 17025) .
[c] No values available in the literature for LiNO$_3$-NaNO$_3$, value taken from [73] for KNO$_3$-NaNO$_3$ (similar PCM compound).

advantages of this concept are that no modification of the RSS is needed and other, possibly expensive, materials to increase heat transfer are spared.

The used PCM is an eutectic mixture of sodium nitrate (NaNO$_3$) and lithium nitrate (LiNO$_3$). The ratio is 15.938 kg NaNO$_3$ to 15.313 kg LiNO$_3$. The two compounds, each purchased with a specified purity of ≥ 99 %, were mixed in solid, powdery state and heated in batches to 350 °C. The relevant PCM material parameters are given in Table 2. The PCM modules were covered in heating mats controlled to 250 °C and filled with liquid PCM to a specified filling level. The resulting PCM mass per module was measured and ranged from 19.00 kg to 19.83 kg, as given in Table 1.

2.2.2. Sensor placement and measurement
The RSS is equipped with sensors for a pressure measurement, a temperature measurement and a differential pressure measurement of the liquid level in the vessel. The charging steam flow is defined by a

pressure measurement in the charging pipe and its specific enthalpy is determined assuming that the steam is saturated.

The PCM modules are instrumented with PT100 temperature sensors in two different arrangements (Type A and Type B). The first type of instrumentation (Type A) includes 36 sensors on different positions as it can be seen on the right side of Fig. 2. One module was instrumented according to Type A instrumentation while the second type of instrumentation (Type B) includes only two sensors. Fig. 2 presents the position of the individual modules on the pressure vessel. All sensors are placed as centrally as possible in the PCM layer. The sensor depth, i.e. the distance from the inner module wall on the RSS side measured in radial direction, is 15 mm for all sensors of the Type B instrumentation. The 36 sensors of the Type A instrumentation are arranged in 12 groups of 3 sensors. Each group includes sensor depths of 8 mm, 15 mm and 25 mm. The total depth of the PCM layer is 30 mm as summarized in Table 1.

The PT100 measurement sensors used have a class A measurement tolerance according to IEC 751 resp. EN 60751 which is defined by $\Delta T = 0 \pm (0.15\,^\circ\mathrm{C} + 0.002 \cdot T)$ at a temperature T in the operation range $-200\,^\circ\mathrm{C} \leq T \leq 600\,^\circ\mathrm{C}$. All sensors were further tested with
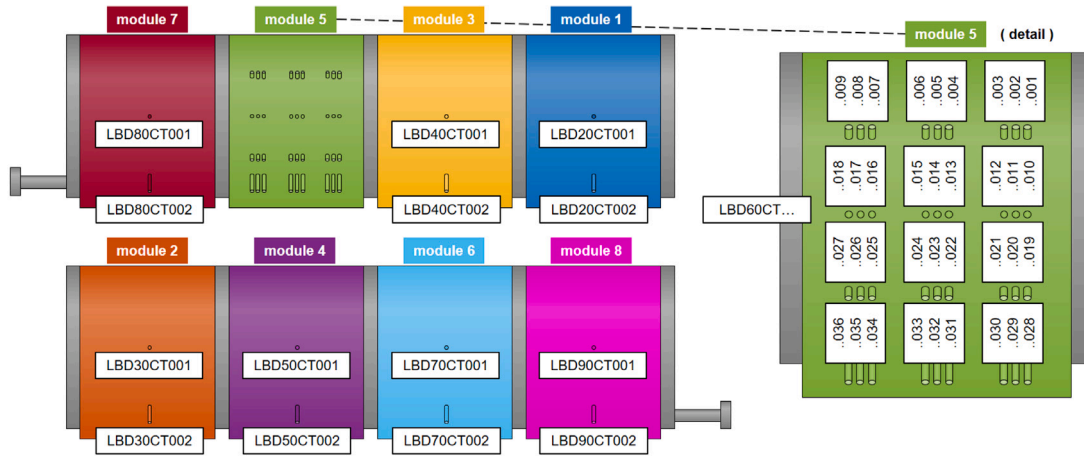
Fig. 2. Temperature measurement setup and sensor denotation in LHTES modules. On the left, the position of the individual modules on the two lateral sides of the pressure vessel is illustrated. On the right, a detailed sketch of the sensor arrangement of the Type A module is presented.
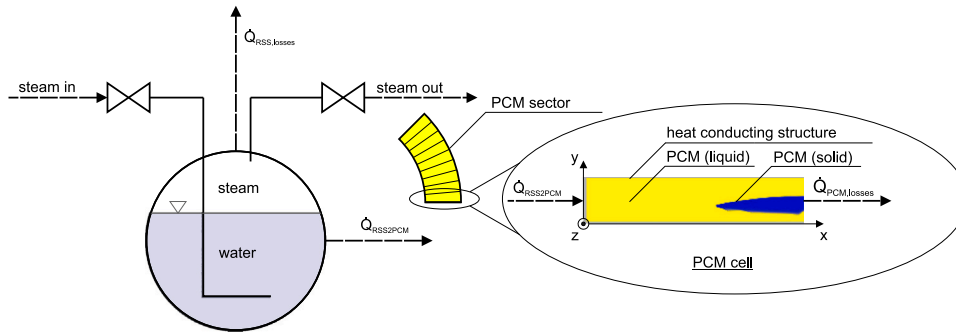

Fig. 3. Schematic illustration of heat flows during hybrid storage charging/discharging.
Source: Reprinted from [67] with permission from Elsevier.

the same calibration device and no significant deviations were found, i.e. deviations of well below $1.0\,°C$.

2.2.3. Control strategy

Charging/discharging of the hybrid storage is only possible via the RSS by injecting/extracting steam or by draining water via the corresponding loading, unloading and purge valves. The PCM attached to the walls of the RSS can be charged/discharged solely by the exchanged heat flows due to the temperature difference. Fig. 3 illustrates steam charging/discharging of the RSS and heat flows between RSS, the LHTES and the environment.

The loading and unloading valves become active when the differential pressure (setpoint to measurement value) exceeds $1.5\,bar$. Furthermore, only either the charging or discharging valve can be active, which means that simultaneous charging and discharging of the storage device is not possible. The purge valve is used to control the filling level of the RSS. When the measured filling level exceeds a certain threshold, the purge valve is activated and water is drained to ensure safe operation of the RSS.

Fig. 4 shows the full hybrid storage prototype setup in the experimental environment.

2.3. RSS modelling

To model an RSS, thermodynamic equilibrium is commonly assumed in literature, see, e.g. Steinmann & Eck [16]. Thereby, the two phases inside the storage vessel, namely water and steam, are considered always in saturated state with both phases at the same temperature. The implemented RSS model is adapted from the validated equilibrium model by Dusek & Hofmann [58].

2.3.1. Governing equations

The variables pressure and temperature, which are directly related in thermodynamic equilibrium, are not sufficient for a complete description of the system. Therefore, another variable is required to fully characterize the state of the system, for example, the specific enthalpy.

The energy and mass balances are expressed as combinations of the two phases (one-dimensional), treating the two phases together as a single fluid mixture. The corresponding governing equations are

$$m_{RSS} \frac{dh_{RSS}}{dt} = \dot{m}_{RSS,in}(h_{RSS,in} - h_{RSS}) + \tag{1}$$

$$\dot{m}_{RSS,out}(h_{RSS,out} - h_{RSS}) + \dot{Q}_{RSS} + V_{RSS} \frac{dp_{RSS}}{dt} \text{ , and}$$

$$V_{RSS} \frac{d\rho_{RSS}}{dt} = \dot{m}_{RSS,in} + \dot{m}_{RSS,out} \text{ .} \tag{2}$$

The steam mass fraction and the corresponding mixing law are defined as

$$x_{RSS} = \frac{m_{RSS,s}}{m_{RSS,s} + m_{RSS,w}} \text{ , and} \tag{3}$$

$$h_{RSS} = x_{RSS} h_{RSS,s} + (1 - x_{RSS}) h_{RSS,w} \text{ .} \tag{4}$$

Therein, m_{RSS}, $\dot{m}_{RSS}$, h_{RSS} and ρ_{RSS} denote the mass, mass flow, specific enthalpy, and density of an equivalent water–steam mixture, respectively. The indices "w" and "s" stands for the water and steam fractions (liquid and vapour phase) and the index additions "in" and "out" denote stream quantities entering and leaving the RSS vessel, respectively. In the assumed saturated state, the pressure p_{RSS} is the same for both phases. The RSS model is considered as an aggregate domain where the balance equations are not further subdivided. The overall volume V_{RSS} is subject to the heat flow

$$\dot{Q}_{RSS} = \dot{Q}_{RSS2PCM} + \dot{Q}_{RSS,loss} \text{ ,} \tag{5}$$
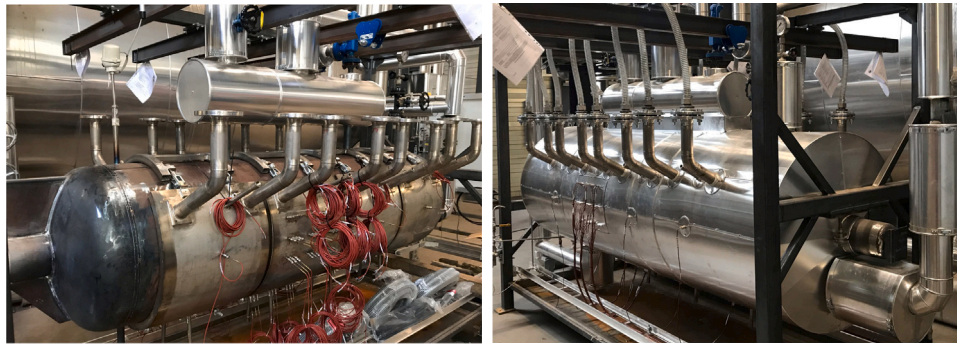
(a) Lab-scale RSS device with LHTES container modules attached to the pressure vessel's surface. The modules are instrumented with PT100 temperature sensors.

(b) Final experimental setup of the hybrid storage prototype, including heat insulation.

Fig. 4. Images of lab-scale hybrid storage prototype in the experimental environment. Photographs by courtesy of AIT Austrian Institute of Technology GmbH.
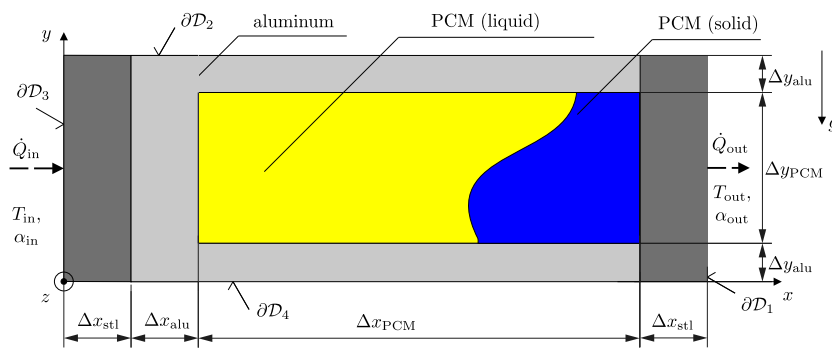

Fig. 5. PCM cell dimensions.

which includes heat losses to the environment $\dot{Q}_{\text{RSS,loss}}$ and the heat flow to the attached PCM modules $\dot{Q}_{\text{RSS2PCM}}$.

2.4. PCM module modelling

We developed a detailed multi-phase thermodynamic model including melting/solidification, heat conduction, and natural convection in two dimensions. The model was developed, successfully validated with experimental data and thoroughly documented in [65,66] and is briefly explained here.

2.4.1. Modelling domain

The PCM modules of the hybrid storage feature an aluminium fin structure orientated in the radial-axial plane of the RSS. Hence, modelling can be reduced to two dimensions when assuming that the depth of the enclosure in z-direction is large enough for wall boundary layer effects to be negligible [66]. Furthermore, an outer diameter of the RSS of $711\,\text{mm}$ is considered large against the full enclosure width in y-direction of $36\,\text{mm}$, thus justifying a rectangular approximation of single fin segments. Fig. 5 illustrates the abstracted fin segment consisting of a rectangular aluminium enclosure filled with PCM. This segment is modelled in local coordinates (x, y) in the two-dimensional spatial domain $\mathcal{D}$ and its boundary $\partial \mathcal{D}$.

2.4.2. Mathematical model

The governing equations within the given assumptions are the energy Eq. (6), continuity Eq. (7) and Navier–Stokes Eqs. (8) as follows:

$$\rho_{\text{PCM}} c \frac{\partial T}{\partial t} = k_{\text{PCM}} \nabla \cdot (\nabla T) - \rho_{\text{PCM}} c (\boldsymbol{u} \cdot \nabla) T \tag{6}$$

$$\nabla \cdot \boldsymbol{u} = 0 \tag{7}$$

$$\rho_{\text{PCM}} \frac{\partial \boldsymbol{u}}{\partial t} + \rho_{\text{PCM}} (\boldsymbol{u} \cdot \nabla) \boldsymbol{u} - \mu \nabla \cdot (\nabla \boldsymbol{u}) = \boldsymbol{f}(T) - \nabla p_{\text{PCM}} \tag{8}$$

Therein, the temperature field $T = T(x, y, t)$ is treated as dependent variable in the energy Eq. (6), and the velocity field $\boldsymbol{u} = [u, v]^T$ with spatial components $u(x, y, t)$ and $v(x, y, t)$ is treated as dependent variable in the Navier–Stokes Eq. (8). The variable p_{PCM} stands for the pressure in the PCM. The symbols ρ_{PCM}, k and μ denote the parameters density, heat conductivity and dynamic viscosity, respectively. Phase change is modelled via the apparent heat capacity method [75], hence the apparent heat capacity

$$c(T) = \begin{cases} c_{\text{S}} & \text{if: } T < T_{\text{m}} - \varepsilon \\ \frac{\Delta l_{\text{m}} + c_{\text{S}} \cdot (T_{\text{m}} + \varepsilon - T) + c_{\text{L}} \cdot (T - (T_{\text{m}} + \varepsilon))}{2\varepsilon} & \text{if: } \begin{matrix} T_{\text{m}} - \varepsilon \leq T \\ T \leq T_{\text{m}} + \varepsilon \end{matrix} \\ c_{\text{L}} & \text{if: } T > T_{\text{m}} + \varepsilon \end{cases} \tag{9}$$

accounts for the latent heat of melting/solidification Δl_{m} in a mushy region ε around the melting temperature T_{m}. The force density $\boldsymbol{f}$ describes the buoyancy force

$$\boldsymbol{f} = \rho \boldsymbol{g} \cong \rho_0 \boldsymbol{g} \left(1 - \beta \left(T - T_{\text{ref}} \right) \right) , \tag{10}$$

which is calculated via the Boussinesq approximation as given in [76] by the volumetric thermal expansion coefficient β, the constant (reference) density ρ_0, a reference temperature T_{ref}, and the gravitational standard acceleration vector $\boldsymbol{g}$.

The time-dependent energy Eq. (6) is discretized using a standard Galerkin finite element approach with four-noded bilinear rectangular elements, and the incompressible Navier–Stokes Eqs. (7)–(8) are solved via finite differences. The obtained velocity field is applied in the next time step of the energy equation. For details, please refer to Kasper (2020) [65].
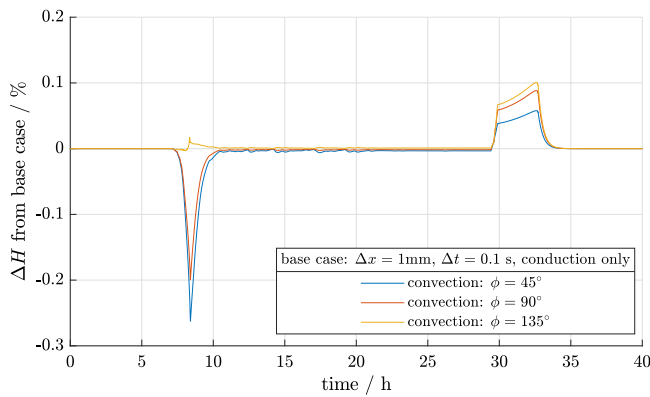
Fig. 6. Deviation of total enthalpy ΔH between simulations of base case (without convection) and including natural convection for different fin orientation angles ϕ of PCM cells under a typical operation scenario. We observed only minor deviations and thus considered only conductive heat transfer in the subsequent analysis.

The symmetry boundaries on the upper and lower side of the domain are treated as adiabatic:

$$q|\partial D_2, \partial D_4 = 0 \tag{11}$$

For the left and right boundaries, Robin boundary conditions,

$$q|\partial D_3 = \alpha_{\text{in}} \cdot (T(x,y,t) - T_{\text{in}}), \tag{12}$$

$$q|\partial D_1 = \alpha_{\text{out}} \cdot (T(x,y,t) - T_{\text{out}}), \tag{13}$$

are prescribed following Newton's law of cooling, where $\alpha_{\text{in}}, \alpha_{\text{out}}$ are the overall heat transfer coefficients, q is the specific heat flux across the boundary, and $T_{\text{in}}, T_{\text{out}}$ present boundary temperatures at the left and right wall surfaces, respectively.

2.4.3. Influence of natural convection

Different fin orientation angles in the LHTES part of the hybrid storage correspond to the inclination of a single PCM cell, as illustrated in Fig. 1. In our studies, we defined the inclination angle ϕ to be 0° when parallel to the gravitational vector, i.e. facing downwards.

While it is often reported that natural convection is negligible during the discharge of LHTES (see, for example [77–79]), it can have significant influence on the charging behaviour [80]. We therefore studied the influence of natural convection on the charging and discharging behaviour of the abstracted single PCM cell for a typical reference operation case and the LHTES geometry and parameters of our prototype (see Fig. 6).

We obtained only slight deviations in total enthalpy and temperature distribution, hence charging/discharging behaviour, between cases modelled with convection at different angles ϕ and the reference case, where convection is neglected. Thus, subsequent analysis, validation and parameter identification was conducted considering only conductive heat transfer in the PCM domain.

2.4.4. Grid size and time step independence

The numerical accuracy implications of the element grid and time step sizes were carefully tested to keep the computational effort in reasonable limits. When natural convection is not considered in the model, a uniformly distributed finite element grid of 1440 elements, corresponding to an element size of $\Delta x = \Delta y = 0.5$ mm proved adequate, as well as a time step size of $\Delta t = 1.0$ s. Further information on grid and time step sensitivity can be found in Appendix A.

2.5. Parameter identification and optimization

Uncertain physical model parameters of the single PCM cell model presented in Section 2.4 were identified via the experimental temperature measurement data of the reference case given in Fig. 12 (exp-II).

The parameter identification procedure aims to find optimal values of the uncertain parameters θ that minimize an objective function $J(\theta)$. The objective function (15) is defined as the RMSE between simulated temperature $\hat{T}(\theta,t)$ and measured temperature $T(t)$ evaluated at n_t points in time.

The optimization problem

$$\tilde{\theta} := arg\left(\min_{\theta} J(\theta)\right) \tag{14}$$

with

$$J(\theta) = \sqrt{\frac{1}{n_t}\sum_{i=1}^{n_t}\left(\hat{T}(t_i,\theta) - T(t_i)\right)^2} \tag{15}$$

is solved in MATLAB® using the Augmented Lagrangian Genetic Algorithm (ALGA) implemented in MATLAB®'s solver *ga* with the maximum number of iterations for the genetic algorithm to perform set to 100, yielding the optimal parameter values $\tilde{\theta}$.

The overall heat transfer coefficients α_{in} and α_{out} are considered the primary source of uncertainty in the PCM cell model, while most of the other parameters can be considered to be accurate. Hence, $\theta = \{\alpha_{\text{in}}, \alpha_{\text{out}}\}$ in the subsequent analysis in Section 3.

3. Results and discussion

3.1. RSS model validation

To validate the RSS model, experiments were conducted using the insulated RSS without the LHTES modules attached. The experiments include dynamic load ramps and closed-valve cool-down tests. The injected and extracted mass flows were determined by balancing calculation using measurements of filling level, total mass, and pressure difference as well as valve characteristics.

Detailed results of the RSS model validation are presented in Appendix B. The experiments provided satisfactory results for the RSS model.

The further experimental setup was designed in such a way that the influence of the LHTES modules on the RSS and the total storage capacity can be identified.

3.2. RSS characterization

Fig. 7 shows the pressure and enthalpy changes of the RSS during exemplary operating scenarios. In this state, no LHTES modules were attached to the RSS before insulation of the pressure vessel.

In the case illustrated in 7(a), the pressure setpoint was increased from 9 bar to 15 bar and after 30 min set to 10 bar. Charging/discharging is completed in roughly 10 min and the maximum feasible power due to enthalpy change is 283 kW. This corresponds to a specific volumetric power of 281 kW m^{-3}. However, it should be noted that the feasible RSS power depends more on the available pressure of the charging steam source and the piping and valve sizes than on the vessel volume. Additionally, a limit on permissible pressure gradients due to safety and durability requirements could further limit the maximum power.

Fig. 7(b) illustrates a test of the full operating range of the RSS, i.e. charging to 23 bar and discharging to 7 bar. During the charging process, 165 MJ of energy were stored in the RSS and 228 MJ were discharged. For typical operating ranges, we characterized the constructed small-scale RSS with a storage capacity of 200 MJ. This corresponds to a volumetric energy density of 198 MJ m^{-3}.
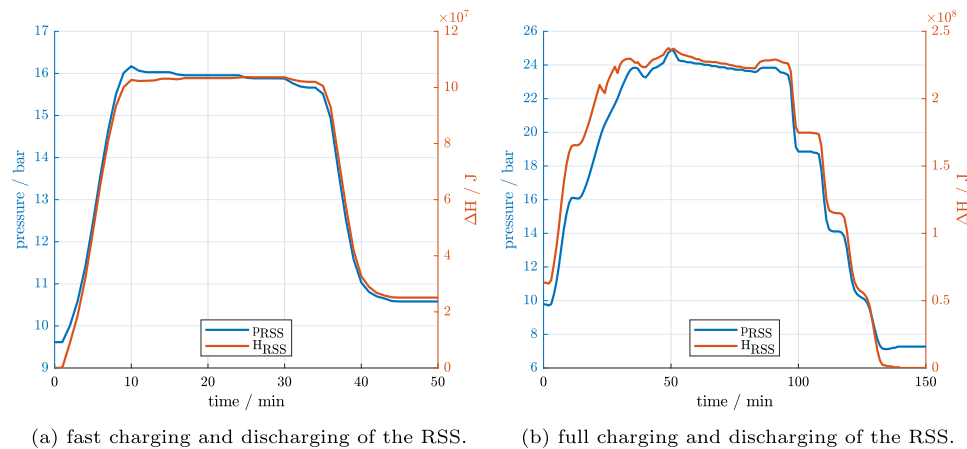
(a) fast charging and discharging of the RSS.

(b) full charging and discharging of the RSS.

Fig. 7. RSS pressure and enthalpy during different operating scenarios without LHTES modules attached.

3.3. General LHTES container module behaviour

3.3.1. Comparison of equal modules

During the experimental investigations, we found significant differences in behaviour, i.e. temperature response, between the eight different modules. Fig. 8 illustrates all measurements of the Type B instrumentation (and corresponding values of the Type A instrumentation) for a 24 h charging scenario. The initial state was stationary and the RSS was held at a pressure of 7 bar, well below the PCM melting point. The RSS was then charged to a pressure of 21 bar, corresponding to a temperature of roughly 217 °C. This pressure was held for 24 h, whereafter it was reduced to a target value of 10 bar.

Comparison of the different LHTES modules in Fig. 8 shows qualitatively similar behaviour during charging and discharging, apart from sensor positions LBD20CT001, LBD80CT001, which show seemingly unphysical behaviour and where thus not considered in further analysis. In fact, the doubtful observation can be explained by a misplaced sensor rod, which did not reach the PCM domain but instead is assumed to record the temperature of the air surrounding the outer side of the adjoining PCM, hence the phase-transition like plateau, well below the actual melting point.

The "quasi-stationary" temperature measurements before the beginning of the charging process, after 24 h of charging and after 18 h hours of discharging show significant differences between modules, which naturally also correlates with charging/discharging power. This discrepancy could be explained by varying effective heat transfer coefficients between RSS and LHTES modules caused by the unequal fitting of the modules to the RSS shell. Since no additional layer to enhance heat transfer was added, the concept relies on the direct contact between the metal surfaces. Even small air gaps in between these surfaces can have immense impact on heat transfer since air features thermal insulating properties. This effect will be discussed in more detail in Section 4.

3.3.2. Comparison of vertical differences

No significant deviation between lower and upper LHTES modules could be obtained, compared to the deviation between different modules on the same horizontal level, see Fig. 8(c). While a tendency of higher measurement values for the upper sensor positions can be obtained, these prove to be on the borderline of significance, as can be seen from the standard deviation plotted in 8(c).

3.3.3. Detailed evaluation of single LHTES module

With the 36 sensors placed in the Type A instrumentation, as described in Section 2.2.2, detailed insight into the single LHTES module is possible (see Fig. 9).

Differences in measurements for different sensor depth proved to be marginal compared to overall variations, that is to say, we obtained a temperature decrease of around 2 °C between the inner most sensor and the outer most sensor, located 8 mm and 25 mm to the inner module wall, respectively. Between the sensors allocated horizontally the difference in the measured temperature is very low, as can be expected. However, differences between sensors allocated vertically are significantly higher though not consistently deviating along one direction along the vertical. This fact suggests uneven heat transfer between RSS and LHTES module, which could be caused by an air gap between these two TES parts.

In light of the results of module comparison presented in Sections 3.3.1 and 3.3.2, we note that the obtained result can by no means be generalized to other modules. Regardless, the insights can be useful for the general interpretation of results and evaluation of the prototype concept, discussed in more detail in Section 4.

3.3.4. Reproducibility of experiments

Naturally, experiment trajectories were repeated several times to ensure reproducibility of the results. Fig. 10 shows comparison between the experiment trajectory introduced in the beginning of this Section, denoted as *exp-I*, and a second run, where it was aimed to reach the same RSS conditions, denoted as *exp-II*, that took place three weeks later. Only minor deviations in temperature measurements can be observed that can be attributed to fluctuations in the RSS temperature trajectory. The experiments were thus considered to be reproducible and their results verifiable.

### 3.4. LHTES model validation and parameter optimization

We used the measurement data from each of the 8 PCM container modules (see Section 2.2.2) to validate the single PCM cell model, outlined in Section 2.4. Uncertain physical model parameters were optimized to fit experimental results, as methodically presented in Section 2.5.

Fig. 11 shows the validation results for three representative sensor positions. Here, only α_{in} and α_{out} were considered as uncertain and optimized to fit the experimental temperature measurement. Table C.6 presents the obtained values as well as the resulting validation errors for the 8 LHTES modules and two sensor positions each.

Additionally, we aimed for improvement of the model fit by allowing the variation of the mushy region temperature range ϵ of the PCM and the specific heat capacities c of PCM and aluminium. The latter two variations did not lead to significant improvement of the results and were thus excluded from further analysis. While allowing larger values of ϵ led to slightly lower absolute root-mean-squared-errors
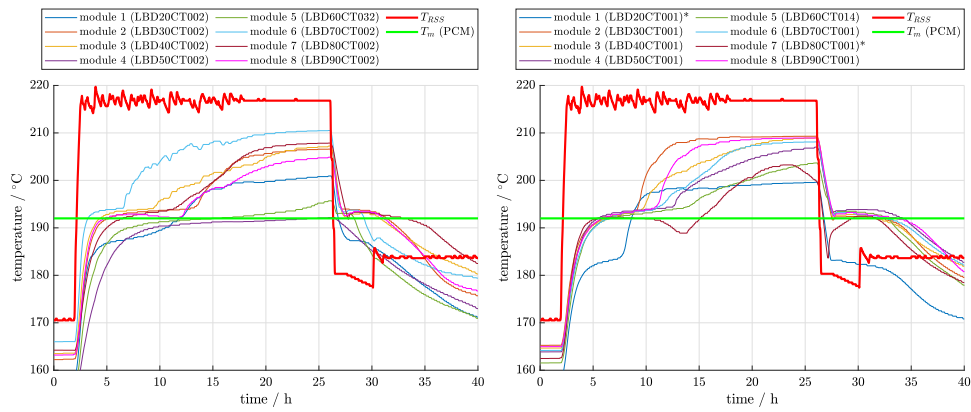
(a) Temperature measurement in RSS and lower sensor positions in LHTES modules.

(b) Temperature measurement in RSS and upper sensor positions in LHTES modules.
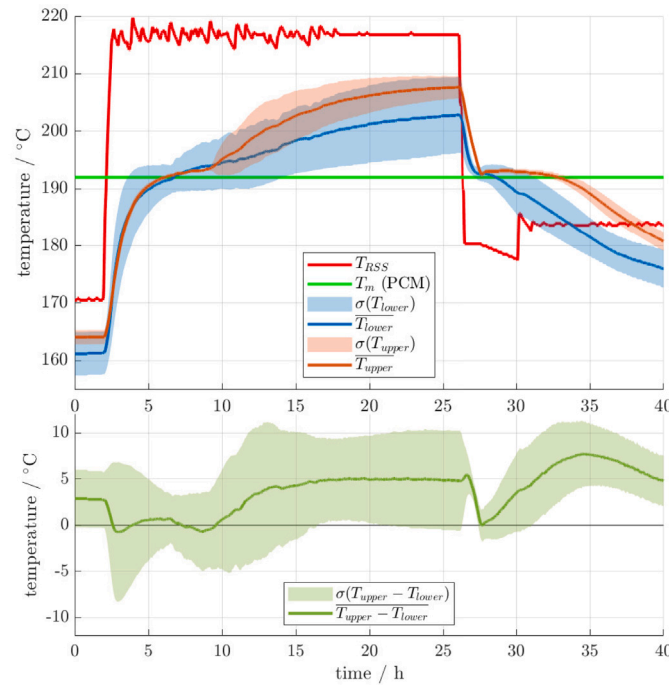
(c) Mean values and corresponding standard deviation of lower T_{lower} and upper sensors T_{upper} for all eight modules respectively (upper figure) and mean value and corresponding standard deviation of the calculated difference between six of the eight sensor pairs ($T_{\text{upper}} - T_{\text{lower}}$).
*Note: modules 1 and 7 were removed from this evaluation, since their measurement values are not representative.

Fig. 8. Comparison of temperature measurement in all eight LHTES container modules during a 24h-charging scenario. We measured striking differences between modules, but only borderline significant deviations between lower and upper sensor positions.

(RMSE), the measurement results indicate a relatively small mushy region temperature range. Thus, also variation of ϵ was dismissed based on qualitative assessment.

With the help of the optimization of α_{in} and α_{out}, satisfactory validation results for used LHTES model were achieved for most sensor positions (e.g. LBD30CT001 in Fig. 11). Charging behaviour is reproduced very well except for minor temporal deviation. During discharging, larger discrepancies can be observed. We assume that further fit improvement is not possible with the presented single PCM cell model within the given framework of assumptions. Remaining deviations could be caused by global heat transfer effects, i.e. intra-cell heat transfer instead of inter-cell heat transfer and possibly disregarded physical effects like, for example, sub-cooling.

The results summarized in Table C.6 show larges deviations between the identified values for the effective heat transfer coefficients of individual LHTES module sectors, in accordance with the results in Section 3.3. The RMSE values between simulated and observed temperature over the whole observation period ranged between $1.8\,°\text{C}$ and $6\,°\text{C}$ for all sensor positions.

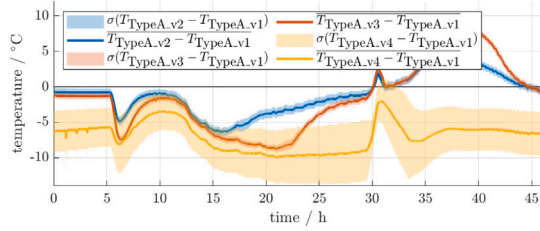### 3.5. Performance analysis of hybrid storage

Performance of the LHTES part of the hybrid storage is characterized by additional storage capacity as well as charging/discharging
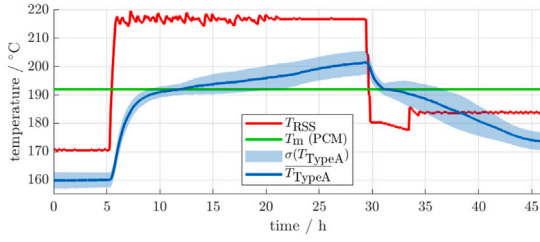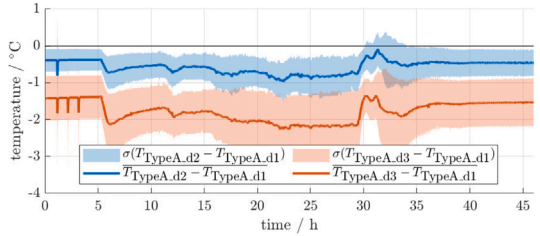
(a) RSS temperature trajectory and mean temperature in Type A LHTES module.
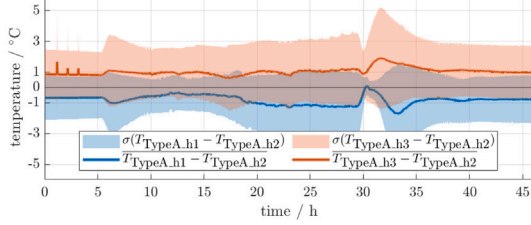
(b) Comparison between sensor measurements allocated horizontally, at the same depth and vertical position.

(c) Comparison between sensor measurements allocated vertically, at the same depth and horizontal position.

(d) Comparison between sensor depth, at the same horizontal and vertical position.

Fig. 9. Detailed analysis of single LHTES module of Type A instrumentation. Temperature measurement deviations between different sensor depths 9(d) and horizontal positions 9(b) behaved as expected and proved to be small, whereas significant deviations are observed between different vertical positions 9(c).

power and duration. The total enthalpy stored within the LHTES modules

$$H = \sum_{i=1}^{n=M} \left(\int_0^{T_i} m_{PCM,i} c_{PCM}(T) \, dT + m_{alu} c_{alu} T_i + m_{stl} c_{stl} T_i \right) \quad (16)$$

is approximated via $M = 16$ temperature measurement points T_i, two for each of the eight modules, replacing the measurement points LBD80CT001 and LBD20CT002, which are considered faulty, by surrogate values of LBD40CT001 and LBD40CT002, respectively. In Eq. (16), c_{alu} and c_{stl} are the specific heat capacities for aluminium and steel, and c_{PCM} is the apparent heat capacity as given in Eq. (9), containing the latent heat Δl_m and the sensible specific heat capacities c_S and c_L of the PCM in the solid and liquid region, respectively. The temperature of each measurement value is assumed constant for half of each LHTES module's mass.
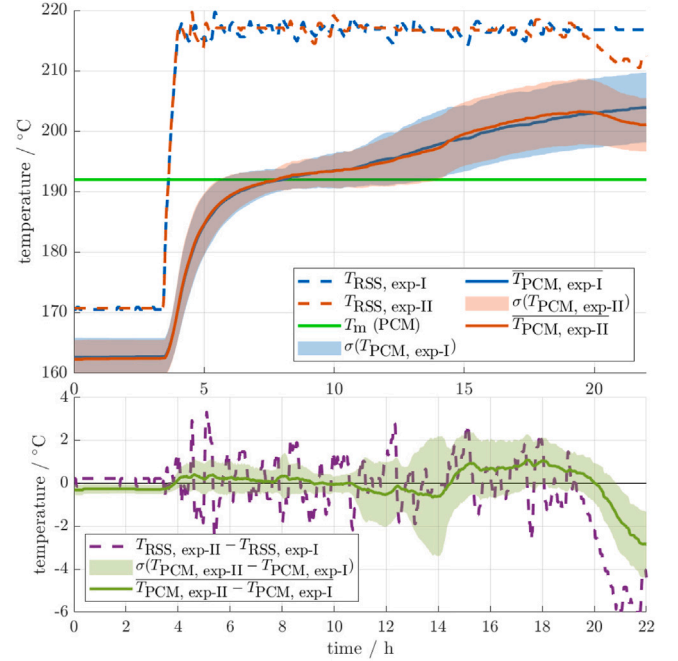

Fig. 10. Comparison of measurement results for two similar charging experiments. Only minor deviations were observed and the experiments were thus considered to be reproducible. *Note: modules 1 and 7 were removed from this evaluation, since their measurement values are not representative.
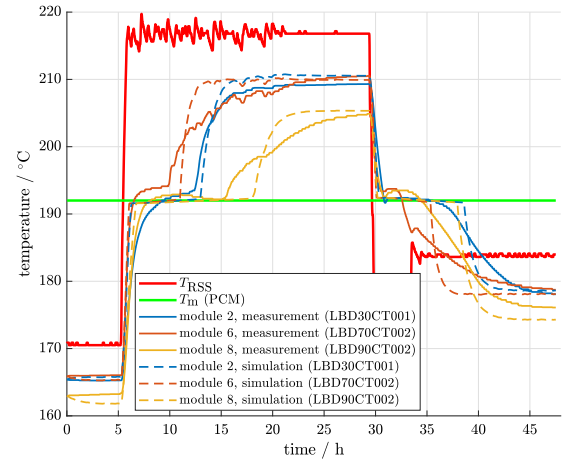

Fig. 11. Validation results of single PCM cell model for three representative sensor positions (LBD30CT001, LBD70CT002, LBD90CT002) and a 24h charging process. Experimental measurements are depicted as solid lines, simulation results are depicted as dashed lines. We obtained satisfactory validation results for most LHTES sensor positions. However, discrepancies are apparent during discharging.

Simulation values are calculated by scaling enthalpy values of the validated single PCM cell models (see, Section 3.4) according to the full LHTES module's mass.

3.5.1. Additional storage capacity by PCM containers

In order to obtain the usable additional storage capacity provided by the LHTES modules, a specific PCM activation test was carried out. In the first experiment (exp-I), the RSS was kept at a constant pressure of 7bar, corresponding to a temperature of roughly 170 °C, which is well below the PCM melting temperature. Thus, it is ensured that no PCM is activated, meaning latent enthalpy stored in the PCM. The RSS was then charged to a value of 21 bar, corresponding to a temperature of approximately 215 °C and immediately afterwards discharged to 7 bar.
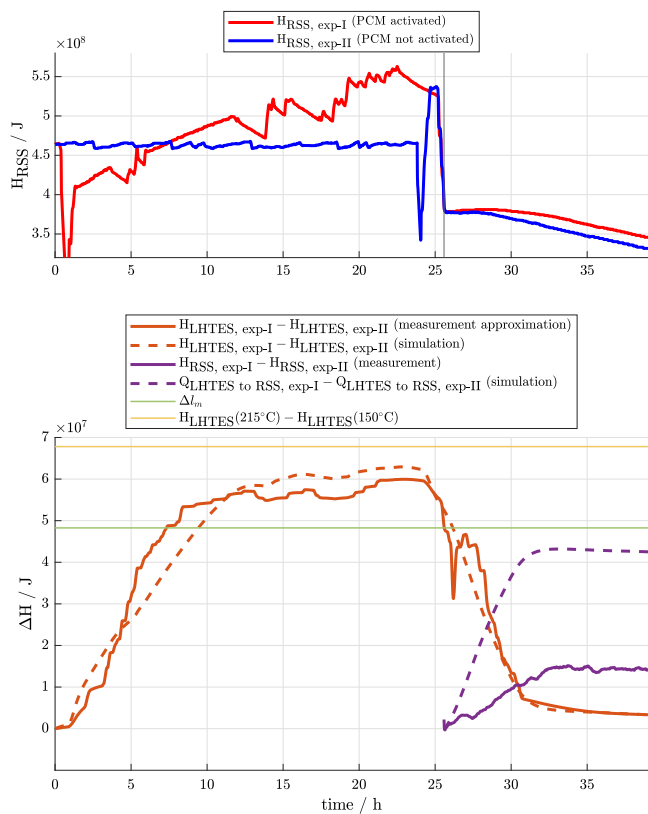
Fig. 12. PCM activation experiments: Enthalpy in the RSS for two different experiment trajectories is plotted in the upper subfigure. In the lower subfigure, additional enthalpy stored in LHTES (solid orange line) and recovered in the RSS during discharging (solid violet line) is plotted. Simulation results are depicted as dashed lines.

Table 3
Mean LHTES power values and duration for the period until 90% of the maximum experimental charging/discharging enthalpy was reached.

		duration h	mean power W	mean specific power W m^{-3}
Charging	(experimental)	11.88	$7.69 \cdot 10^4$	$5.60 \cdot 10^5$
	(simulation)	10.45	$8.78 \cdot 10^4$	$6.40 \cdot 10^5$
Discharging	(experimental)	7.85	$-1.10 \cdot 10^5$	$-8.02 \cdot 10^5$
	(simulation)	8.65	$-1.01 \cdot 10^5$	$-7.36 \cdot 10^5$

3.5.2. Charging/discharging power characterization

Power values estimated by experimental temperature measurements are prone to strong fluctuations, caused by RSS pressure measurement fluctuations and the nature of enthalpy estimation. Therefore, we introduced a mean power value, which is calculated for the duration until 90% of the maximum experimental charging/discharging enthalpy was reached. Hence, quantitative comparison of both charging/discharging power and duration is enabled between experimental observations and different simulation scenarios. For the evaluation presented here and illustrated in Fig. 13, typical operation scenarios were assumed, as already introduced in Section 3.5.1. During charging, the RSS' target pressure was set to 21 bar, corresponding to a temperature of roughly 217 °C. During discharging, the RSS' target pressure was set to 10 bar, corresponding to a temperature of roughly 184 °C.

The results for the obtained mean LHTES power values are given in Table 3. Fig. 13 shows the charging and discharging power characterization of the LHTES part of the hybrid storage via both power estimated by experimental measurements and power deduced from multiple single PCM cell simulations.

We observed good agreement between the simulated and measured values for mean power and charging/discharging duration. The charging duration is slightly underestimated by the simulation, while discharging duration is slightly overestimated compared to the experimental values. Discharging is faster than charging for this trajectory, i.e. the absolute value of discharging power is higher than the charging power, since undesired heat losses of the LHTES accelerate the discharging process.

Table 4 presents mean LHTES power values and charging duration for simulations with different reference cells scaled to the full LHTES storage mass. The rather low LHTES power rates and long time periods are a result of low heat transfer values (see Table C.6) between the RSS and the LHTES in this first hybrid storage prototype, and, relative to that, high heat losses to the environment. While we expected that heat transfer between the RSS and the LHTES part of the hybrid storage prototype is very critical to overall performance, it proved to be even more difficult to manage than initially expected. This fact is also reflected in the surprisingly strong deviating temporal behaviour between the eight LHTES modules, which are identical in construction, as presented in Section 3.3.

3.6. Sensitivity analysis of key process parameters

With the help of the validated single PCM cell models, we carried out a sensitivity analysis on the influence of the critical process parameters α_{in} and α_{out} on the key process parameters charging/discharging duration and power (see Fig. 14). The large dependency of the boundary heat transfer coefficients on the charging duration is apparent.

To put the measurement results into perspective, we consider the "theoretical" optimum values for the heat transfer coefficients assuming direct contact, i.e. perfect heat transfer between solid construction elements. We assume a heat transfer coefficient from liquid water inside the RSS to its steel shell of 700 W m^{-2} K^{-1} as given in [64,81], perfect heat transfer between the RSS' steel shell and the PCM containers' steel shell and heat conduction in the PCM container's steel walls according to the material properties and geometry values given in Tables 1 and 2, respectively. Furthermore, we assume a typical heat conductivity

All valves of the RSS were then closed and temperature and pressure inside the RSS was monitored for another 24 h. In a second experiment (exp-II), the RSS was kept at a constant pressure of 21 bar for 24 h, thus ensuring that all PCM is fully activated, i.e. liquefied. All valves of the RSS were then closed as in exp-I.

Fig. 12 shows relative enthalpy values stored in the RSS for exp-I (red) and exp-II (blue) in the upper part of the figure and the RSS enthalpy difference between exp-I and exp-II in the lower part of the figure. An approximation of the enthalpy difference in the PCM is depicted in the orange line.

Since the approximation based on PCM temperature measurement points given in Eq. (16) is prone to a large error, additional data guidelines were added, indicating the total available latent enthalpy (green) and the total enthalpy difference between 215 °C and 150 °C LHTES module temperature (yellow). These values equal 48.3 MJ and 67.8 MJ, respectively. The approximate enthalpy stored in the LHTES part was 60 MJ. During discharging, the enthalpy difference in the RSS between activated and not activated PCM reached a maximum value of 15.1 MJ after 8.5 h of discharging. We can deduce from this experiment that approximately 26% of the stored enthalpy in the LHTES could be recovered in the RSS during a discharging period of 8.5 h. The 60 MJ of achieved storage capacity corresponds to a volumetric energy density of 437 MJ m^{-3}. Note that this value differs from the volumetric phase change enthalpy of the pure PCM compound, valued at 716 MJ m^{-3}, since the LHTES' full module volume and temperature operating range is considered. The LHTES storage capacity amounts to 30% of the RSS storage capacity valued at 200 MJ in Section 3.2 and the LHTES features 221% of the RSS' energy density. The total energy density of the hybrid storage amounts to 227 MJ m^{-3}.

Agreement of the simulation values with the experimental observations (see Fig. 12) are considered satisfactory.

(a) LHTES charging power
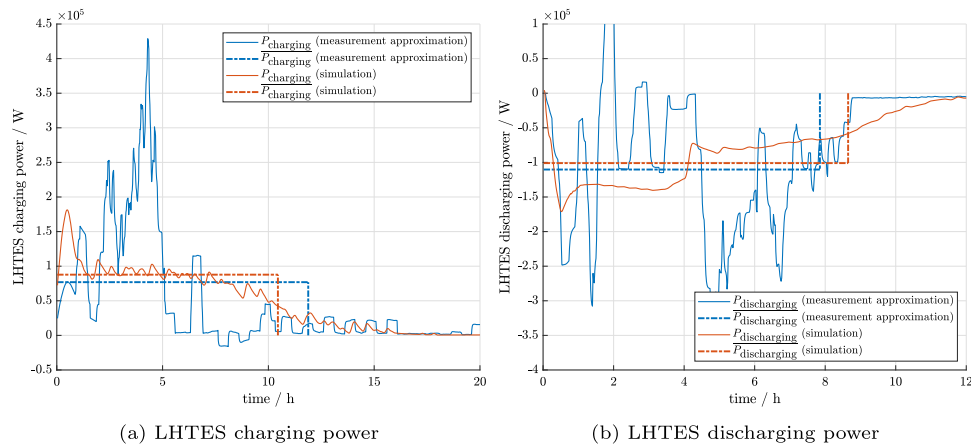

(b) LHTES discharging power

Fig. 13. Charging and discharging power characterization of the LHTES part of the hybrid storage. Experimental values (blue) are calculated via the enthalpy estimated by Eq. (16). Simulation values are calculated via the validated LHTES module parameters. Dashed-dotted lines represent the mean power values for the duration until 90% of the maximum experimental charging/discharging enthalpy was reached.
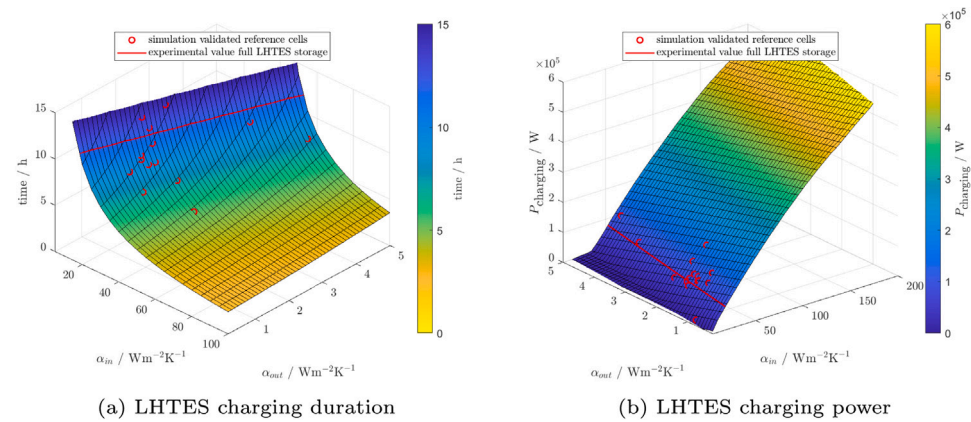

(a) LHTES charging duration

(b) LHTES charging power

Fig. 14. LHTES charging duration and power for varying values of the critical heat transfer coefficients α_{in} and α_{out}. Simulation values of the validated reference cells scaled to the full LHTES mass are illustrated as red circles. The experimental measurement value of the full LHTES storage is given as red isoline.

Table 4
Mean LHTES power values and duration for the period until 90% of the maximum experimental charging/discharging enthalpy was reached for simulation of different reference cells. The power values were scaled to the full LHTES storage mass.

Sensor identifier	charging_duration h	mean_power W	mean_specific_power W m^{-3}
LBD20CT001	7.70	$1.19 \cdot 10^5$	$8.67 \cdot 10^5$
LBD30CT001	7.73	$1.26 \cdot 10^5$	$9.15 \cdot 10^5$
LBD40CT001	9.01	$1.02 \cdot 10^5$	$7.40 \cdot 10^5$
LBD50CT001	7.67	$1.19 \cdot 10^5$	$8.71 \cdot 10^5$
LBD60CT014	13.47	$6.79 \cdot 10^4$	$4.95 \cdot 10^5$
LBD70CT001	10.02	$9.13 \cdot 10^4$	$6.66 \cdot 10^5$
LBD80CT001[a]	13.50	$6.78 \cdot 10^4$	$4.94 \cdot 10^5$
LBD90CT001	8.92	$1.03 \cdot 10^5$	$7.48 \cdot 10^5$
LBD20CT002[a]	10.12	$9.05 \cdot 10^4$	$6.59 \cdot 10^5$
LBD30CT002	10.68	$8.57 \cdot 10^4$	$6.24 \cdot 10^5$
LBD40CT002	9.05	$1.01 \cdot 10^5$	$7.38 \cdot 10^5$
LBD50CT002	38%[b]	$2.45 \cdot 10^4$	$1.79 \cdot 10^5$
LBD60CT032	14.57	$6.28 \cdot 10^4$	$4.58 \cdot 10^5$
LBD70CT002	5.38	$1.70 \cdot 10^5$	$1.24 \cdot 10^6$
LBD80CT002	9.65	$9.49 \cdot 10^4$	$6.91 \cdot 10^5$
LBD90CT002	11.85	$7.72 \cdot 10^4$	$5.63 \cdot 10^5$

[a]Measurements not representative due to experimental errors, see Section 3.3.1.
[b]Only 38% of charging capacity reached.

value for compressed mineral wool of $0.045 \, \text{W m K}^{-1}$ for the $100 \, \text{mm}$ insulation layer and a heat transfer coefficient of $5 \, \text{W m}^{-2}\text{K}^{-1}$ from this insulation layer to the environment. These assumptions correspond to scenario 3 in Table 5. Under these assumptions, we arrive at

$597.49 \, \text{W m}^{-2} \, \text{K}^{-1}$ for the maximum, i.e. best possible, value of α_{in} and $0.41 \, \text{W m}^{-2} \, \text{K}^{-1}$ for the minimum, i.e. best possible, value of α_{out}.

While the assumption of perfect contact between the RSS' and the PCM containers' steel shell delivers "theoretical" benchmarks for fast charging/discharging and large power values, these are unlikely to be reached. Hence, we consider another scenario (scenario 4 in Table 5) where heat transfer enhancement via a small layer of heat conductivity paste between the two storage types is achieved. Assuming that this layer is $5 \, \text{mm}$ wide and filled with typical high temperature heat conductivity paste with a heat conductivity value of $3 \, \text{W m K}^{-1}$, we arrive at an overall heat transfer coefficient of α_{in} and $299.37 \, \text{W m}^{-2} \, \text{K}^{-1}$.

Table 5 lists the resulting charging/discharging duration and mean power of these scenarios together with simulation values of the actual LHTES prototype and the best achieved LHTES values. These results show that charging/discharging times can be reduced by up to 10 times and specific power could be increased by up to 10 and 5 times, respectively compared to the achieved values. Therefore, feasible ways to enhance heat transfer between the RSS' steel shell and the LHTES containers' steel shell, i.e. α_{in} have to be found.

The hybrid storage prototype construction, as presented in Section 2.2.1, relies on direct contact between the two storage types, i.e. between two metallic surfaces of cylindrical shape. With the heat conductivity of still air being as low as $0.038 \, \text{W m K}^{-1}$, small gaps of around $1 \, \text{mm}$ width lead to a crucial drop in overall heat transfer. Fig. 15 illustrates the dependency of the overall heat transfer coefficient α_{in} on the width of a gap between the RSS' steel shell and the LHTES containers' shell.

Table 5

Calculation of mean LHTES power values and duration, for the period until 90% of the maximum experimental charging/discharging enthalpy was reached, for different scenarios. Scenario 1 corresponds to the mean value of validated LHTES modules of the built prototype, as given in Table 3. Scenario 2 corresponds to the best validated LHTES module (based on sensor LBD70CT002) scaled to the full prototype mass. Scenario 3 assumes perfect heat transfer conditions. Scenario 4 considers a design iteration with, again, perfect heat transfer conditions but a layer of heat conductivity paste between RSS and LHTES modules.

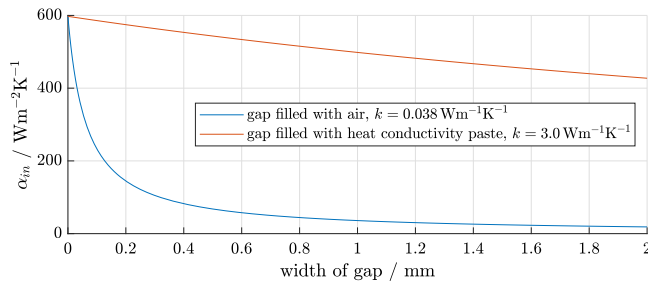| scenario	$\frac{\alpha_{in}}{\mathrm{Wm^{-2}K^{-1}}}$	$\frac{\alpha_{out}}{\mathrm{Wm^{-2}K^{-1}}}$	$\frac{\mathrm{duration}}{\mathrm{h}}$	$\frac{\mathrm{mean\ power}}{\mathrm{W}}$	$\frac{\mathrm{mean\ specific\ power}}{\mathrm{Wm^{-3}}}$
1 (charging)	–	–	11.88	$7.69 \cdot 10^4$	$5.60 \cdot 10^5$
1 (discharging)			7.85	$-1.10 \cdot 10^5$	$-8.02 \cdot 10^5$
2 (charging)	29.61	1.42	5.38	$1.70 \cdot 10^5$	$1.24 \cdot 10^6$
2 (discharging)			5.50	$-1.58 \cdot 10^5$	$-1.15 \cdot 10^6$
3 (charging)	597.49	0.41	0.77	$1.24 \cdot 10^6$	$9.04 \cdot 10^6$
3 (discharging)			1.28	$-6.93 \cdot 10^5$	$-5.05 \cdot 10^6$
4 (charging)	299.37	0.41	1.08	$8.60 \cdot 10^5$	$6.27 \cdot 10^6$
4 (discharging)			1.87	$-4.72 \cdot 10^5$	$-3.44 \cdot 10^6$

Fig. 15. Theoretic dependency of the overall heat transfer coefficient α_{in} on the width of an assumed gap between the RSS steel shell and the attached LHTES module, filled with still air (blue line) and filled with heat conductivity paste (orange line).

It should be noted that more research on the technical feasibility of the proposed application of heat conductivity paste (scenario 4) is necessary. While some suppliers offer non-hardening high-temperature compounds (e.g., silicon-based pastes such as Omegatherm 201 or Silicon Solutions SS-240), compound integrity under cycling operation must be tested. Furthermore, economic viability of the holistic concept (see, e.g., Niknam & Sciacovelli [62]) could be strongly influenced by the costs of such modification.

4. Conclusion

4.1. Summary of results

We presented the first-of-a-kind functional lab-scale prototype of the novel hybrid RSS/LHTES storage concept presented by Dusek & Hofmann [56,57]. While previous investigations focused on numerical characterization and techno-economic assessments, we delivered the first technically feasible construction and experimental investigation of such hybrid storage. The RSS could be retrofitted with additional 60 MJ storage capacity by means of LHTES modules. This corresponds to a storage capacity increase of 30% compared to the lab-scale RSS unit, which features a capacity of 200 MJ in the typical operating range. The retrofitted LHTES features a volumetric energy density of $437 \mathrm{\,MJ\,m^{-3}}$, which is 221% of the RSS' energy density. The total energy density of the hybrid storage amounts to $227 \mathrm{\,MJ\,m^{-3}}$.

Charging/discharging times and specific thermal power of the LHTES modules were roughly measured as 8 h/ 12 h and $560 \mathrm{\,W k\,m^{-3}}$ / $-802 \mathrm{\,kW\,m^{-3}}$, respectively, in the typical operation region. During the PCM activation experiments, approximately 26% of the stored enthalpy in the LHTES could be retrieved back to the RSS.

Numerical models for both RSS and LHTES part of the hybrid storage were validated with satisfactory results. Via parameter optimization, the effective heat transfer coefficients α_{in} and α_{out} were identified individually for different LHTES module sectors. The RMSE

values between simulated and observed temperature over the whole observation period ranged between $1.8\,°C$ and $6\,°C$ for all sensor positions. Qualitatively, charging behaviour of the LHTES is reproduced very well except for minor temporal deviations while larger discrepancies in the discharging behaviour can be observed.

With the help of our validated thermal model, a sensitivity analysis of the key process parameters on the hybrid storage performance was carried out. The results show that specific charging/discharging power could be increased by up to 10 and 5 times compared to the achieved values with realistic re-adjustment of heat transfer between RSS and LHTES part, e.g., by using a layer of high temperature heat conductivity paste or similar concepts.

4.2. Outlook on future research and development

The hybrid storage prototype realized in this experimental investigation is very promising for industrial application due to its easy retrofit procedure. However, the investigations have shown that heat transfer between RSS and LHTES must be improved further to increase charging/discharging power and heat recovery. In the developed construction concept, direct contact between the RSS and the LHTES containers is essential for efficient storage operation. Fixed, permanent mounting to the RSS shell was disregarded due to technical and safety restrictions given in detail in Section 2.1. Unfortunately, the metallic springs, intended to ensure a tight fit of LHTES containers to the RSS surface, proved inadequate.

Future iterations of this hybrid storage could include high-temperature heat-conducting paste, thermal oil or other heat transfer compounds between the two storage parts in order to eliminate the possibility of air gaps. Such re-adjustments were not considered in the present study for the sake of simplicity, due to safety concerns, and because of limited resources to invest in both costly material and time to investigate additional safety issues introduced with such compounds.

A fundamentally different approach of flexible LHTES container designs mounted on the RSS should also be considered and re-evaluated. For example, construction by means of injection molding or additive manufacturing could provide essential advantages compared to the solid steel body construction in the present prototype. Such a container design could, as the presented prototype, maintain high safety requirements and technical constraints of operating a steam vessel. The use of flexible elastomer-based encapsulations of PCM, e.g., as developed by Yu et al. [82] or Li et al. [83], to allow for thermal expansion could provide essential benefits, if heat conductivity of the encapsulation material is sufficiently high. Wu et al. [84] developed polymer and graphite based highly thermally conductive, form-stable, flexible and leakage-proof phase change composites that are also promising for application in the TES use case targeted in our work. However, most research focuses on micro-scale encapsulation of PCM and temperature ranges below pressurized steam applications. The combined properties of flexibility, high heat conductivity and thermal stability [85] for macro-scale encapsulation have not been optimized for widespread

use, yet. Furthermore, more research on the interaction of the combined setup under operating conditions is necessary to optimize hybrid storage performance.

Our experimental analysis of this first-of-a-kind hybrid RSS/LHTES storage presents guidelines for future development of hybrid storage applications. Ultimately, future retrofit hybrid thermal energy storage concepts should become efficient, economically viable and accepted in industry and thus a key part to overcome the ever-increasing problem of mismatch between energy supply and demand.

CRediT authorship contribution statement

Lukas Kasper: Data curation, Formal analysis, Investigation, Methodology, Software, Validation, Visualization, Writing – original draft, Writing – review & editing. **Dominik Pernsteiner:** Investigation, Methodology, Software, Writing – review & editing. **Alexander Schirrer:** Conceptualization, Formal analysis, Investigation, Methodology, Writing – review & editing. **Stefan Jakubek:** Conceptualization, Funding acquisition, Supervision. **René Hofmann:** Conceptualization, Funding acquisition, Methodology, Supervision, Writing – review & editing.

Declaration of competing interest

The authors declare that they have no known competing financial interests or personal relationships that could have appeared to influence the work reported in this paper.

Data availability

Data will be made available on request.

Appendix A. Grid and time step size sensitivity of numerical PCM model

As presented in Section 2.4.4, a uniformly distributed finite element grid of 1440 elements, corresponding to an element size of $\Delta x = \Delta y = 0.5\,\text{mm}$, and a time step size of $\Delta t = 1.0\,\text{s}$ proved adequate for the numerical PCM simulations in this work.

For sensitivity analysis of grid an time step size, a typical simulation case, representative for the results in this paper, was chosen. The grid size sensitivity is illustrated for a reference simulation case in Fig. A.1. The time step size sensitivity is illustrated in Fig. A.2. Comparison was made by means of total enthalpy deviation to a base case, since this metric is of major importance to the numerical studies in this paper. Both figures show fast convergence and indicate that further refinement of the chosen values has no significant impact on the simulation results.

Appendix B. Validation of RSS model

Here, more details on the RSS model validation presented in Section 3.1 can be found. Fig. B.3 presents the most characteristic values for the RSS model validation in six subfigures for a given pressure setpoint trajectory.
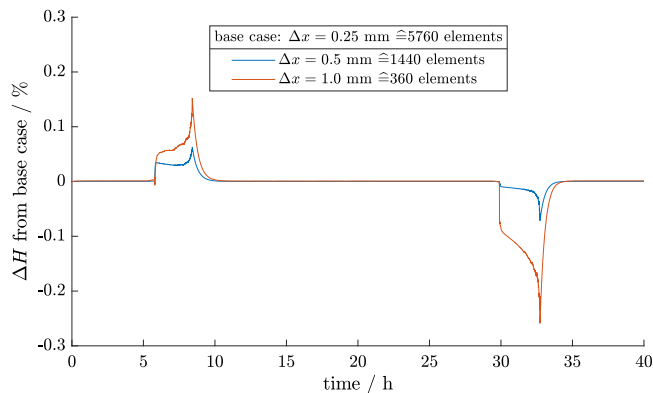

Fig. A.1. Grid size sensitivity of reference case, carried out with a time step size $\Delta t = 0.1\,\text{s}$.
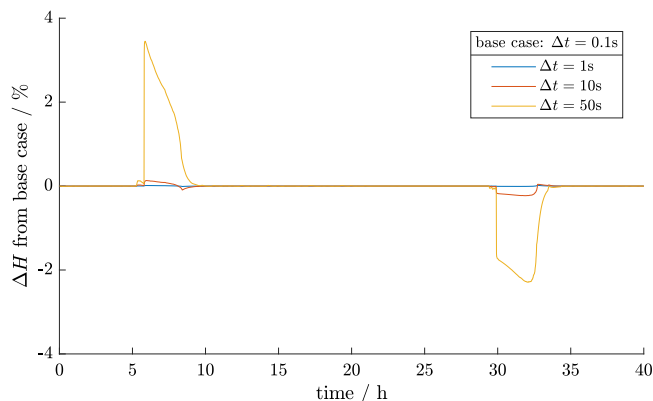

Fig. A.2. Time step sensitivity of reference case, carried out with a grid size of 5760 elements, corresponding to an element size of $\Delta x = \Delta y = 0.25\,\text{mm}$.

Table C.6
Validation results of single PCM cell model for different sensor positions for the reference case given in Fig. 11. The uncertain physical parameters α_{in} and α_{out} (column two and three) were optimized to fit the measurement data. Column four and five present the obtained absolute RMSE and maximal error, respectively, between the measured and simulated temperature trajectory in the observed period.

Sensor identifier	$\frac{\alpha_{\text{in}}}{\text{Wm}^{-2}\text{K}^{-1}}$	$\frac{\alpha_{\text{out}}}{\text{Wm}^{-2}\text{K}^{-1}}$	$\frac{\text{RMSE}}{\text{K}}$	$\frac{\text{max. error}}{\text{K}}$
LBD20CT001	45.70	3.79	4.0	10.4
LBD30CT001	30.28	1.72	1.8	6.4
LBD40CT001	33.27	1.65	3.1	5.2
LBD50CT001	8.15	0.83	2.2	7.6
LBD60CT014	48.76	5.02	5.1	14.3
LBD70CT001	51.49	1.81	2.6	6.0
LBD80CT001[a]	30.16	1.40	3.4	10.9
LBD90CT001	28.4	1.73	2.3	6.8
LBD20CT002[a]	59.11	4.77	5.7	19.5
LBD30CT002	35.80	1.15	2.1	10.9
LBD40CT002	32.33	1.50	3.3	9.7
LBD50CT002	40.42	1.91	6.0	13.4
LBD60CT032	26.24	1.63	2.8	8.9
LBD70CT002	29.61	1.42	3.1	10.7
LBD80CT002	29.34	2.16	3.6	8.8
LBD90CT002	29.72	1.08	2.1	10.4

[a]Measurements not representative due to experimental errors, see Section 3.3.1.

Appendix C. Detailed results of single PCM cell model validation

Table C.6 presents the obtained values as well as the resulting validation errors for the 8 LHTES modules and two sensor positions each.
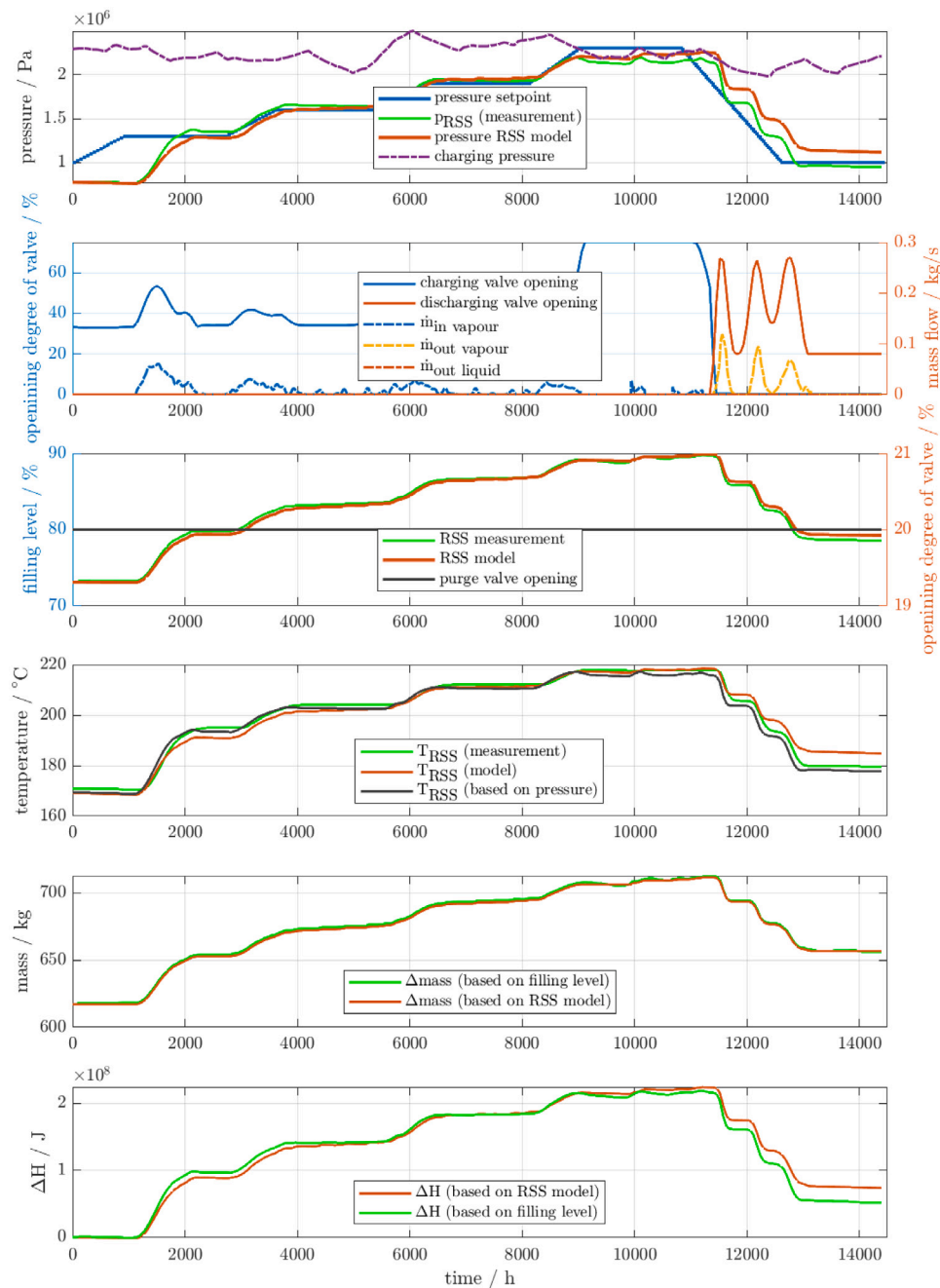
Fig. B.3. RSS measurement values and model outputs for a given pressure setpoint trajectory.

References

[1] Leonard MD, Michaelides EE, Michaelides DN. Energy storage needs for the substitution of fossil fuel power plants with renewables. Renew Energy 2020;145:951–62. http://dx.doi.org/10.1016/j.renene.2019.06.066.

[2] Cabeza LF. 2 - Advances in thermal energy storage systems: methods and applications. In: Cabeza LF, editor. Advances in thermal energy storage systems (Second Edition). Woodhead Publishing Series in Energy, second ed.. Woodhead Publishing; 2021, p. 37–54. http://dx.doi.org/10.1016/B978-0-12-819885-8.00002-4.

[3] Arce P, Medrano M, Gil A, Oró E, Cabeza LF. Overview of thermal energy storage (TES) potential energy savings and climate change mitigation in Spain and Europe. Appl Energy 2011;88(8):2764–74. http://dx.doi.org/10.1016/j.apenergy.2011.01.067.

[4] Borri E, Zsembinszki G, Cabeza LF. Recent developments of thermal energy storage applications in the built environment: A bibliometric analysis and systematic review. Appl Therm Eng 2021;189:116666. http://dx.doi.org/10.1016/j.applthermaleng.2021.116666.

[5] Cabeza LF, de Gracia A, Zsembinszki G, Borri E. Perspectives on thermal energy storage research. Energy 2021;231:120943. http://dx.doi.org/10.1016/j.energy.2021.120943.

[6] Beck A, Sevault A, Drexler-Schmid G, Schöny M, Kauko H. Optimal Selection of Thermal Energy Storage Technology for Fossil-Free Steam Production in the Processing Industry. Appl Sci 2021;11(3). http://dx.doi.org/10.3390/app11031063.

[7] Alva G, Lin Y, Fang G. An overview of thermal energy storage systems. Energy 2018;144:341–78. http://dx.doi.org/10.1016/j.energy.2017.12.037.

[8] Therkelsen P, McKane A. Implementation and rejection of industrial steam system energy efficiency measures. Energy Policy 2013;57:318–28. http://dx.doi.org/10.1016/j.enpol.2013.02.003.

[9] Rathgeber C, Lävemann E, Hauer A. Economic top–down evaluation of the costs of energy storages—A simple economic truth in two equations. J Energy Storage 2015;2:43–6. http://dx.doi.org/10.1016/j.est.2015.06.001.

[10] Halmschlager D, Beck A, Knöttner S, Koller M, Hofmann R. Combined optimization for retrofitting of heat recovery and thermal energy supply in industrial systems. Appl Energy 2022;305:117820. http://dx.doi.org/10.1016/j.apenergy.2021.117820.

[11] Gibb D, Johnson M, Gasia JRJ, Cabeza LF, Seitz A. Process integration of thermal energy storage systems – Evaluation methodology and case studies. Appl Energy 2018;230:750–60. http://dx.doi.org/10.1016/j.apenergy.2018.09.001.

[12] Einstein D, Worrell E, Khrushch M. Steam systems in industry: Energy use and energy efficiency improvement potentials. Lawrence Berkeley National Laboratory 2001. . Retrieved from https://escholarship.org/uc/item/3m1781f1.

[13] Yang M, Dixon RK. Investing in efficient industrial boiler systems in China and Vietnam. Energy Policy 2012;40:432–7. http://dx.doi.org/10.1016/j.enpol.2011.10.030, Strategic Choices for Renewable Energy Investment.

[14] IEA. Tracking industrial energy efficiency and CO2 emissions. (OECD) Organisation for Economic Co-operation and Development; 2007, ISBN: 978-92-64-03016-9.

[15] González-Gómez P, Laporte-Azcué M, Fernández-Torrijos M, Santana D. Hybrid storage solution steam-accumulator combined to concrete-block to save energy during startups of combined cycles. Energy Convers Manage 2022;253:115168. http://dx.doi.org/10.1016/j.enconman.2021.115168.

[16] Steinmann W-D, Eck M. Buffer storage for direct steam generation. Sol Energy 2006;80(10):1277–82. http://dx.doi.org/10.1016/j.solener.2005.05.013, Solar Power and Chemical Energy Systems (SolarPACES'04).

[17] González-Roubaud E, Pérez-Osorio D, Prieto C. Review of commercial thermal energy storage in concentrated solar power plants: Steam vs. molten salts. Renew Sustain Energy Rev 2017;80:133–48. http://dx.doi.org/10.1016/j.rser.2017.05.084.

[18] Biglia A, Comba L, Fabrizio E, Gay P, Ricauda Aimonino D. Steam batch thermal processes in unsteady state conditions: Modelling and application to a case study in the food industry. Appl Therm Eng 2017;118:638–51. http://dx.doi.org/10.1016/j.applthermaleng.2017.03.004.

[19] Kuravi S, Trahan J, Goswami DY, Rahman MM, Stefanakos EK. Thermal energy storage technologies and systems for concentrating solar power plants. Prog Energy Combust Sci 2013;39(4):285–319. http://dx.doi.org/10.1016/j.pecs.2013.02.001.

[20] Goldstern W. Steam storage installations: construction, design, and operation of industrial heat accumulators, vol. 4. Pergamon; 1970.

[21] Stevanovic VD, Maslovaric B, Prica S. Dynamics of steam accumulation. Appl Therm Eng 2012;37:73–9. http://dx.doi.org/10.1016/j.applthermaleng.2012.01.007.

[22] Biglia A, Comba L, Fabrizio E, Gay P, Ricauda Aimonino D. Steam batch thermal processes in unsteady state conditions: Modelling and application to a case study in the food industry. Appl Therm Eng 2017;118. http://dx.doi.org/10.1016/j.applthermaleng.2017.03.004.

[23] Ibrahim NI, Al-Sulaiman FA, Rahman S, Yilbas BS, Sahin AZ. Heat transfer enhancement of phase change materials for thermal energy storage applications: A critical review. Renew Sustain Energy Rev 2017;74:26–50. http://dx.doi.org/10.1016/j.rser.2017.01.169.

[24] Mehling H, Cabeza LF. Heat and cold storage with PCM. Springer Berlin Heidelberg; 2008, http://dx.doi.org/10.1007/978-3-540-68557-9.

[25] Dincer I, Rosen M. Thermal energy storage: systems and applications. John Wiley & Sons; 2002, URL https://books.google.at/books?id=EsfcWE5lX40C.

[26] Bista S, Hosseini SE, Owens E, Phillips G. Performance improvement and energy consumption reduction in refrigeration systems using phase change material (PCM). Appl Therm Eng 2018;142:723–35. http://dx.doi.org/10.1016/j.applthermaleng.2018.07.068.

[27] Zalba B, Marín JM, Cabeza LF, Mehling H. Review on thermal energy storage with phase change: materials, heat transfer analysis and applications. Appl Therm Eng 2003;23(3):251–83. http://dx.doi.org/10.1016/S1359-4311(02)00192-8.

[28] Nguyen T-T, Martin V, Malmquist A, Silva CA. A review on technology maturity of small scale energy storage technologies. In: Goodfield D, editor. Renew Energy Environ Sustain 2017;2:36. http://dx.doi.org/10.1051/rees/2017039.

[29] Cabeza LF, Martorell I, Miró L, Fernández AI, Barreneche C, Cabeza LF, Fernández AI, Barreneche C. 1 - Introduction to thermal energy storage systems. In: Cabeza LF, editor. Advances in thermal energy storage systems (Second Edition). Woodhead Publishing Series in Energy, second ed.. Woodhead Publishing; 2021, p. 1–33. http://dx.doi.org/10.1016/B978-0-12-819885-8.00001-2.

[30] Merlin K, Delaunay D, Soto J, Traonvouez L. Heat transfer enhancement in latent heat thermal storage systems: Comparative study of different solutions and thermal contact investigation between the exchanger and the PCM. Appl Energy 2016;166:107–16. http://dx.doi.org/10.1016/j.apenergy.2016.01.012.

[31] Yang X, Lu Z, Bai Q, Zhang Q, Jin L, Yan J. Thermal performance of a shell-and-tube latent heat thermal energy storage unit: Role of annular fins. Appl Energy 2017;202:558–70. http://dx.doi.org/10.1016/j.apenergy.2017.05.007.

[32] Eslamnezhad H, Rahimi AB. Enhance heat transfer for phase-change materials in triplex tube heat exchanger with selected arrangements of fins. Appl Therm Eng 2017;113:813–21. http://dx.doi.org/10.1016/j.applthermaleng.2016.11.067.

[33] Augspurger M, Choi K, Udaykumar H. Optimizing fin design for a PCM-based thermal storage device using dynamic Kriging. Int J Heat Mass Transfer 2018;121:290–308. http://dx.doi.org/10.1016/j.ijheatmasstransfer.2017.12.143.

[34] Muhammad M, Badr O. Performance of a finned, latent-heat storage system for high temperature applications. Appl Therm Eng 2017;116:799–810. http://dx.doi.org/10.1016/j.applthermaleng.2017.02.006.

[35] Motahar S, Khodabandeh R. Experimental study on the melting and solidification of a phase change material enhanced by heat pipe. Int Commun Heat Mass Transfer 2016;73:1–6. http://dx.doi.org/10.1016/j.icheatmasstransfer.2016.02.012.

[36] Mesalhy O, Lafdi K, Elgafy A, Bowman K. Numerical study for enhancing the thermal conductivity of phase change material (PCM) storage using high thermal conductivity porous matrix. Energy Convers Manage 2005;46(6):847–67. http://dx.doi.org/10.1016/j.enconman.2004.06.010.

[37] Motahar S, Nikkam N, Alemrajabi AA, Khodabandeh R, Toprak MS, Muhammed M. A novel phase change material containing mesoporous silica nanoparticles for thermal storage: A study on thermal conductivity and viscosity. Int Commun Heat Mass Transfer 2014;56:114–20. http://dx.doi.org/10.1016/j.icheatmasstransfer.2014.06.005.

[38] Khodadadi J, Hosseinizadeh S. Nanoparticle-enhanced phase change materials (NEPCM) with great potential for improved thermal energy storage. Int Commun Heat Mass Transfer 2007;34(5):534–43. http://dx.doi.org/10.1016/j.icheatmasstransfer.2007.02.005.

[39] Yang J, Qi G-Q, Bao R-Y, Yi K, Li M, Peng L, Cai Z, Yang M-B, Wei D, Yang W. Hybridizing graphene aerogel into three-dimensional graphene foam for high-performance composite phase change materials. Energy Storage Mater 2018;13:88–95. http://dx.doi.org/10.1016/j.ensm.2017.12.028.

[40] Huang X, Xia W, Zou R. Nanoconfinement of phase change materials within carbon aerogels: phase transition behaviours and photo-to-thermal energy storage. J Mater Chem A 2014;2:19963–8. http://dx.doi.org/10.1039/C4TA04605F.

[41] Min P, Liu J, Li X, An F, Liu P, Shen Y, Koratkar N, Yu Z-Z. Thermally Conductive Phase Change Composites Featuring Anisotropic Graphene Aerogels for Real-Time and Fast-Charging Solar-Thermal Energy Conversion. Adv Funct Mater 2018;28(51):1805365. http://dx.doi.org/10.1002/adfm.201805365.

[42] Aftab W, Mahmood A, Guo W, Yousaf M, Tabassum H, Huang X, Liang Z, Cao A, Zou R. Polyurethane-based flexible and conductive phase change composites for energy conversion and storage. Energy Storage Mater 2019;20:401–9. http://dx.doi.org/10.1016/j.ensm.2018.10.014.

[43] Wu S, Li T, Tong Z, Chao J, Zhai T, Xu J, Yan T, Wu M, Xu Z, Bao H, Deng T, Wang R. High-Performance Thermally Conductive Phase Change Composites by Large-Size Oriented Graphite Sheets for Scalable Thermal Energy Harvesting. Adv Mater 2019;31(49):1905099. http://dx.doi.org/10.1002/adma.201905099.

[44] Wu M, Li T, Wang P, Wu S, Wang R, Lin J. Dual-Encapsulated Highly Conductive and Liquid-Free Phase Change Composites Enabled by Polyurethane/Graphite Nanoplatelets Hybrid Networks for Efficient Energy Storage and Thermal Management. Small 2022;18(9):2105647. http://dx.doi.org/10.1002/smll.202105647.

[45] Zayed ME, Zhao J, Li W, Elsheikh AH, Elbanna AM, Jing L, Geweda A. Recent progress in phase change materials storage containers: Geometries, design considerations and heat transfer improvement methods. J Energy Storage 2020;30:101341. http://dx.doi.org/10.1016/j.est.2020.101341.

[46] Wu M, Wu S, Cai Y, Wang R, Li T. Form-stable phase change composites: Preparation, performance, and applications for thermal energy conversion, storage and management. Energy Storage Mater 2021;42:380–417. http://dx.doi.org/10.1016/j.ensm.2021.07.019.

[47] Abdelsalam M, Sarafraz P, Cotton J, Lightstone M. Heat transfer characteristics of a hybrid thermal energy storage tank with Phase Change Materials (PCMs) during indirect charging using isothermal coil heat exchanger. Sol Energy 2017;157:462–76. http://dx.doi.org/10.1016/j.solener.2017.08.043.

[48] Zhao J, Ji Y, Yuan Y, Zhang Z, Lu J. Energy-Saving Analysis of Solar Heating System with PCM Storage Tank. Energies 2018;11(1). http://dx.doi.org/10.3390/en11010237.

[49] Frazzica A, Manzan M, Sapienza A, Freni A, Toniato G, Restuccia G. Experimental testing of a hybrid sensible-latent heat storage system for domestic hot water applications. Appl Energy 2016;183:1157–67. http://dx.doi.org/10.1016/j.apenergy.2016.09.076.

[50] Underwood C, Shepherd T, Bull S, Joyce S. Hybrid thermal storage using coil-encapsulated phase change material. Energy Build 2018;159:357–69. http://dx.doi.org/10.1016/j.enbuild.2017.10.095.

[51] Cabeza LF, nez MI, Solé C, Roca J, Nogués M. Experimentation with a water tank including a PCM module. Sol Energy Mater Sol Cells 2006;90(9):1273–82. http://dx.doi.org/10.1016/j.solmat.2005.08.002.

[52] Zauner C, Hengstberger F, Mörzinger B, Hofmann R, Walter H. Experimental characterization and simulation of a hybrid sensible-latent heat storage. Appl Energy 2017;189:506–19. http://dx.doi.org/10.1016/j.apenergy.2016.12.079.

[53] Tatsidjodoung P, Le Pierrès N, Luo L. A review of potential materials for thermal energy storage in building applications. Renew Sustain Energy Rev 2013;18:327–49. http://dx.doi.org/10.1016/j.rser.2012.10.025.

[54] Buschle J, Steinmann W-D, Tamme R. Latent heat storage for process heat applications. In: 10th International conference on thermal energy storage ECOSTOCK 2006, vol. 31. 2006, p. 1–8, URL https://elib.dlr.de/55379/,

[55] Tamme R, Bauer T, Buschle J, Laing D, Müller-Steinhagen H, Steinmann W-D. Latent heat storage above 120°C for applications in the industrial process heat sector and solar power generation. Int J Energy Res 2008;32(3):264–71. http://dx.doi.org/10.1002/er.1346.

[56] Dusek S, Hofmann R. A hybrid energy storage concept for future application in industrial processes. Therm Sci 2018;22:2235–42. http://dx.doi.org/10.2298/TSCI171230270D.

[57] Dusek S, Hofmann R. A Hybrid Storage Concept for Improving Classical Ruth's Type Steam Accumulators. In: Proceedings of the 12th SDEWES Conference, Dubrovnic, Croatia. 2017, p. 4–8.

[58] Dusek S, Hofmann R. Modeling of a Hybrid Steam Storage and Validation with an Industrial Ruths Steam Storage Line. Energies 2019;12(6). http://dx.doi.org/10.3390/en12061014.

[59] Fang M, Chen G. Effects of different multiple PCMs on the performance of a latent thermal energy storage system. Appl Therm Eng 2007;27(5):994–1000. http://dx.doi.org/10.1016/j.applthermaleng.2006.08.001.

[60] Li W, Zhang Y, Zhang X, Zhao J. Studies on performance enhancement of heat storage system with multiple phase change materials. J Energy Storage 2021;103585. http://dx.doi.org/10.1016/j.est.2021.103585.

[61] Nepustil U, Laing-Nepustil D, Lodemann D, Sivabalan R, Hausmann V. High Temperature Latent Heat Storage with Direct Electrical Charging – Second Generation Design. Energy Procedia 2016;99:314–20. http://dx.doi.org/10.1016/j.egypro.2016.10.121, 10th International Renewable Energy Storage Conference, IRES 2016, 15-17 March 2016, Düsseldorf, Germany.

[62] Niknam PH, Sciacovelli A. Hybrid PCM-steam thermal energy storage for industrial processes – Link between thermal phenomena and techno-economic performance through dynamic modelling. Appl Energy 2023;331:120358. http://dx.doi.org/10.1016/j.apenergy.2022.120358.

[63] Hofmann R, Dusek S, Gruber S, Drexler-Schmid G. Design Optimization of a Hybrid Steam-PCM Thermal Energy Storage for Industrial Applications. Energies 2019;12(5). http://dx.doi.org/10.3390/en12050898.

[64] Dusek S, Hofmann R, Gruber S. Design analysis of a hybrid storage concept combining Ruths steam storage and latent thermal energy storage. Appl Energy 2019;251:113364. http://dx.doi.org/10.1016/j.apenergy.2019.113364.

[65] Kasper L. Modeling of the phase change material of a hybrid storage using the finite element method. TU Wien Academic Press; 2020, http://dx.doi.org/10.34727/2020/isbn.978-3-85448-037-2.

[66] Kasper L, Pernsteiner D, Koller M, Schirrer A, Jakubek S, Hofmann R. Numerical studies on the influence of natural convection under inclination on optimal aluminium proportions and fin spacings in a rectangular aluminium finned latent-heat thermal energy storage. Appl Therm Eng 2021;190:116448. http://dx.doi.org/10.1016/j.applthermaleng.2020.116448.

[67] Pernsteiner D, Kasper L, Schirrer A, Hofmann R, Jakubek S. Co-simulation methodology of a hybrid latent-heat thermal energy storage unit. Appl Therm Eng 2020;178:115495. http://dx.doi.org/10.1016/j.applthermaleng.2020.115495.

[68] Pernsteiner D, Schirrer A, Kasper L, Hofmann R, Jakubek S. Data-based model reduction for phase change problems with convective heat transfer. Appl Therm Eng 2021;184:116228. http://dx.doi.org/10.1016/j.applthermaleng.2020.116228.

[69] Pernsteiner D, Schirrer A, Kasper L, Hofmann R, Jakubek S. State estimation concept for a nonlinear melting/solidification problem of a latent heat thermal energy storage. Comput Chem Eng 2021;153:107444. http://dx.doi.org/10.1016/j.compchemeng.2021.107444.

[70] Gasia J, Miró L, Cabeza LF. Review on system and materials requirements for high temperature thermal energy storage. Part 1: General requirements. Renew Sustain Energy Rev 2017;75:1320–38. http://dx.doi.org/10.1016/j.rser.2016.11.119.

[71] HyStEPs │ NEFI URL https://www.nefi.at/en/project/hysteps.

[72] Pereira da Cunha J, Eames P. Thermal energy storage for low and medium temperature applications using phase change materials – A review. Appl Energy 2016;177:227–38. http://dx.doi.org/10.1016/j.apenergy.2016.05.097.

[73] Vogel J, Felbinger J, Johnson M. Natural convection in high temperature flat plate latent heat thermal energy storage systems. Appl Energy 2016;184:184–96. http://dx.doi.org/10.1016/j.apenergy.2016.10.001.

[74] thyssenkrupp: Stainless Steel datasheets . Retrieved from https://www.thyssenkrupp-materials.co.uk/stainless-steel-316ti-14571.html.

[75] Tenchev R, Mackenzie J, Scanlon T, Stickland M. Finite element moving mesh analysis of phase change problems with natural convection. Int J Heat Fluid Flow 2005;26(4):597–612. http://dx.doi.org/10.1016/j.ijheatfluidflow.2005.03.003, CHT'04.

[76] Huang M, Eames P, Norton B. Comparison of a small-scale 3D PCM thermal control model with a validated 2D PCM thermal control model. Sol Energy Mater Sol Cells 2006;90(13):1961–72. http://dx.doi.org/10.1016/j.solmat.2006.02.001.

[77] Medrano M, Yilmaz M, Nogués M, Martorell I, Roca J, Cabeza LF. Experimental evaluation of commercial heat exchangers for use as PCM thermal storage systems. Appl Energy 2009;86(10):2047–55. http://dx.doi.org/10.1016/j.apenergy.2009.01.014.

[78] Seddegh S, Wang X, Henderson AD. A comparative study of thermal behaviour of a horizontal and vertical shell-and-tube energy storage using phase change materials. Appl Therm Eng 2016;93:348–58. http://dx.doi.org/10.1016/j.applthermaleng.2015.09.107.

[79] Longeon M, Soupart A, Fourmigué J-F, Bruch A, Marty P. Experimental and numerical study of annular PCM storage in the presence of natural convection. Appl Energy 2013;112:175–84. http://dx.doi.org/10.1016/j.apenergy.2013.06.007.

[80] Mostafavi Tehrani SS, Diarce G, Taylor RA. The error of neglecting natural convection in high temperature vertical shell-and-tube latent heat thermal energy storage systems. Sol Energy 2018;174:489–501. http://dx.doi.org/10.1016/j.solener.2018.09.048.

[81] Herr H. Wärmelehre: Technische Physik Band 3. Europa-Lehrmittel; 1994.

[82] Yu D-H, He Z-Z. Shape-remodeled macrocapsule of phase change materials for thermal energy storage and thermal management. Appl Energy 2019;247:503–16. http://dx.doi.org/10.1016/j.apenergy.2019.04.072.

[83] Li W-W, Cheng W-L, Xie B, Liu N, Zhang L-S. Thermal sensitive flexible phase change materials with high thermal conductivity for thermal energy storage. Energy Convers Manage 2017;149:1–12. http://dx.doi.org/10.1016/j.enconman.2017.07.019.

[84] Wu S, Li T, Wu M, Xu J, Hu Y, Chao J, Yan T, Wang R. Highly thermally conductive and flexible phase change composites enabled by polymer/graphite nanoplatelet-based dual networks for efficient thermal management. J Mater Chem A 2020;8:20011–20. http://dx.doi.org/10.1039/D0TA05904H.

[85] Jacob R, Bruno F. Review on shell materials used in the encapsulation of phase change materials for high temperature thermal energy storage. Renew Sustain Energy Rev 2015;48:79–87. http://dx.doi.org/10.1016/j.rser.2015.03.038.

[86] Hofmann R, Zauner C, Dusek S, Hengsberger F. DAMPFSPEICHER EU Patent 3 260 803 A1. 2017, URL https://patents.google.com/patent/EP3260803A1.